國　立　交　通　大　學

電子工程學系　電子研究所碩士班

碩　士　論　文

以偵測循環字首類型為重點之 LTE 初始下行同步

Initial Downlink Synchronization for LTE Systems with Emphasis on Detection of Cyclic Prefix Type

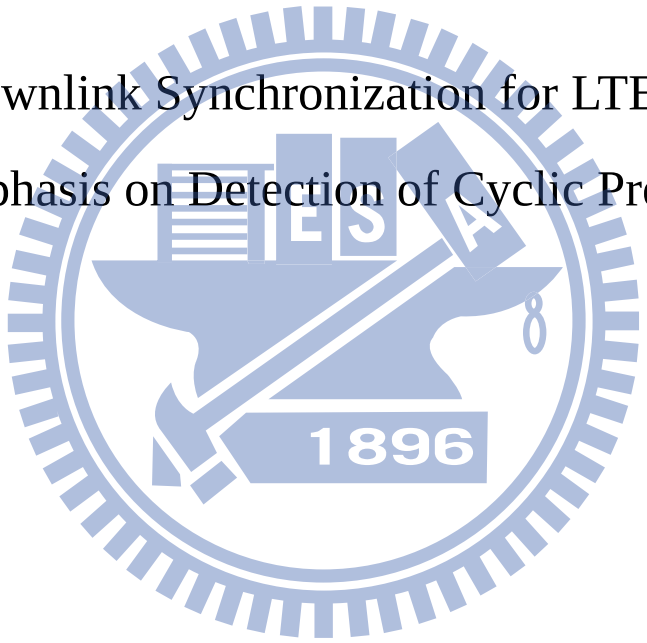

研 究 生： 謝男鑫

指導教授： 林大衛 教授

中 華 民 國 一〇二 年 八 月

以偵測循環字首類型為重點之 LTE 初始下行同步

Initial Downlink Synchronization for LTE Systems with Emphasis on Detection of Cyclic Prefix Type

研 究 生: 謝男鑫　　Student: Nan-Shin Hsieh

指導教授: 林大衛　　Advisor: Dr. David W. Lin

國 立 交 通 大 學

電子工程學系　　電子研究所碩士班

碩 士 論 文

A Thesis

Submitted to Department of Electronics Engineering & Institute of Electronics

College of Electrical and Computer Engineering

National Chiao Tung University

in Partial Fulfillment of the Requirements

for the Degree of Master of Science

in

Electronics Engineering

August 2013

Hsinchu, Taiwan, Republic of China

中 華 民 國 一〇二 年 八 月

以偵測循環字首類型為重點之 LTE 初始下行同步

研究生：謝男鑫　　指導教授：林大衛 博士

國立交通大學

電子工程學系 電子研究所碩士班

摘要

本篇論文介紹LTE-A系統裡關於初始下行同步的問題，包括問題陳述、演算法推導、以及程式模擬。在初始下行同步中，我們發展了一套同步估測演算法，包括了符元時間偏移、載波偏移和訊號傳輸所使用的循環字首類型。首先，我們建立了LTE-A系統下的傳送端和接收端的訊號模型，然後基於最大可能性估測(maximum likelihood)法推導其解。此解不僅於可加性白色高斯雜訊(additive white Gaussian noise, AWGN)、單一路徑瑞利衰減(single-path Rayleigh fading)通道下在具有普遍正確性，且也適用於多路徑衰減(multipath fading)通道。為了大幅減低計算複雜度，我們在處理載波偏移過程中做一近似，雖然在多路徑衰減通道下此解為次優解，但因為此近似在可加性白色高斯雜訊和單一路徑瑞利衰減通道下不影響估測程序，所以在這些通道下亦為最佳解。

在模擬部分，我們設計出一個合理的LTE-A系統接收訊號模型，在可加性白色高斯雜訊通道下得到的數據驗證此演算法，然後在多路徑衰減通道傳輸中使用數種不同多路徑通道、相對移動車速以及雜訊比來測試此演算法對這些環境下所產生的結果。

Initial Downlink Synchronization for LTE Systems with Emphasis on Detection of Cyclic Prefix Type

Student: Nan-Shin Hsieh Advisor: Dr. David W. Lin

Department of Electronics Engineering
& Institute of Electronics
National Chiao Tung University

Abstract

This thesis introduces the topic about initial downlink synchronization, including problem formulation, algorithm derivation and program simulation, in LTE-A system. We develop an algorithm about the joint estimation of symbol timing offset (STO), carrier frequency offset (CFO), and detection of the cyclic prefix (CP) type used in signal transmission. We first establish the transmitted and received signal models of LTE-A system and then derive the solution based on the maximum likelihood (ML) criterion. It is a general solution over not only additive white Gaussian noise (AWGN) and single-path Rayleigh fading channels but also multipath fading channels. In estimating CFO, we consider an approximation so as to reduce computational complexity largely. Though it is the suboptimal solution under multipath fading channels, it is an optimal solution under AWGN and single-path Rayleigh fading channels because the approximate term has no effect on estimation process.

In simulation, we establish a reasonable received signal model in LTE-A system, and then simulate our proposed estimator under AWGN channel to verify its performance. Moreover, we test it under single-path Rayleigh fading and different multipath fading channels, including Standford University Interim (SUI) and Pedestrian B (PB), at different mobility and different signal to noise ratio (SNR).

誌謝

這篇論文能夠順利完成，首先要感謝的是我的指導教授林大衛老師，在這兩年的研究生涯裡，老師總是很細心、用心的指導我，使得我學習到不少研究的精神與方法。

此外，感謝王柏森學長、柯俊言學長、李政憲學長、梁晉源學長給予我在研究過程上的指導與建議。還有感謝葆崧、夏銘、信宏，很幸運可以跟你們在同一實驗室，能和你們共同討論、分享生活上的點點滴滴，讓這兩年的研究生涯充滿許多的歡樂與寶貴的回憶。謝謝通訊電子與訊號處理實驗室所有的成員，志堯、鈞凱、哲瑋、長廷、琬瑜、暐翔、子傑、明孝、中威、家駿以及學弟妹們。謝謝碩二的室友們，家麟、夏銘、執中，每晚回到寢室總是可以開心的閒聊，忘記一天下來的疲憊。

最後，我要感謝我的家人，感謝他們一直都在背後支持我，在求學過程中總是不斷的鼓勵我，讓我有幹勁的繼續向前邁進。

在此，將此篇論文獻給所有陪伴我走過這一段歲月、幫助過我的貴人們。

謝男鑫

民國一百零二年 於新竹

Contents

1 Introduction **1**

2 Overview of the LTE-A Downlink Standard **3**

2.1 OFDM and OFDMA Basics 3

2.1.1 Discrete-time baseband OFDM system model 3

2.1.2 Cyclic prefix 4

2.1.3 OFDMA 5

2.2 Overview of LTE and LTE-A Downlink Specifications 6

2.2.1 Frame structure 7

2.2.2 Slot structure and physical resources 7

2.2.3 Random access 9

2.2.4 Cell search 10

2.2.5 Zadoff-Chu (ZC) sequences 11

2.2.6 Primary synchronization signal (PSS) 12

2.2.7 Secondary synchronization signal (SSS) 12

2.2.8 Broadcast channel (BCH) 15

3 Initial Downlink Synchronization **17**

3.1 The Initial Downlink Synchronization Problem 17

3.1.1 Transmission system model 17

3.1.2 The ML approach to synchronization 21

3.2 Solution of the ML Estimation Problem 21
3.2.1 Derivation of the likelihood function for extended CP 21
3.2.2 Derivation of the likelihood function for normal CP 31
3.2.3 Joint estimation of STO, CFO, and CP type 32

4 Simulation Results and Analysis **36**
4.1 Simulation Conditions 36
4.2 Simulation Method 39
4.3 CP Type Estimation Performance with A Small Observation Window 40
4.3.1 AWGN and Single-Path Rayleigh Fading Channels 40
4.3.2 Multipath Fading Channels 43
4.4 CP Type Estimation Performance Under Different Observation Window Sizes 43

5 Conclusion and Future Work **56**
5.1 Conclusion 56
5.2 Future Work 57

Bibliography **58**

List of Figures

2.1 Baseband OFDM transmitter and receiver. 4

2.2 OFDM symbols with CP. 5

2.3 Types of resource allocation in OFDMA system (modified from [3, Fig. 4.29]). 5

2.4 Frame structure type 1 [1, Fig.4.1-1]. 7

2.5 Frame structure type 2 [1, Fig. 4.2-1]. 7

2.6 Slot structure for normal and extended CP [2, Fig. 8.3]. 8

2.7 Detailed signal structure for normal CP [1, Figs. 5.2.1-1 and 6.2.2-1], [2, Fig. 8.2]. 8

2.8 Random access procedure [2, Figure 10.1]. 10

2.9 downlink frame structure for the type of normal CP. 11

2.10 PSS mapping in the frequency domain (modified from [2, Figure 9.4]). 12

2.11 SSS mapping in the frequency domain (modified from [2, Figure 9.5]). 15

2.12 BCH transmission chain processing [2, Figure 9.6]. 15

2.13 PBCH mapping (modified from [2, Figure 9.7]). 16

3.1 Transmission system structure. 18

3.2 Slot structure in the time domain. 18

3.3 Structure of the autocorrelation matrix $\mathbf{C}_r$. 24

3.4 Moving average. 24

3.5 Autocorrelation matrix example. 25

3.6 Three-region data correlation. 26

3.7 Relative positioning of observation window with respect to STO, as well as the correlation structure in the received signal. 27

4.1 Tap location adjustment by rounding to integer sample spacing. 39

4.2 Error performance of CP type detection in AWGN channel with window size $2N_{fft} + 1N_{512}$. 41

4.3 Error performance of CP type detection in single-path Rayleigh fading channel at different speeds with window size $2N_{fft} + 1N_{512}$. 41

4.4 Window sliding structure. 42

4.5 Pairs of data correlated with window size $2N_{fft} + 1N_{512}$. 42

4.6 Error performance of CP type detection in SUI1 channel at different speeds with window size $2N_{fft} + 1N_{512}$. 43

4.7 Error performance of CP type detection in SUI2 channel at different speeds with window size $2N_{fft} + 1N_{512}$. 44

4.8 Error performance of CP type detection in SUI3 channel at different speeds with window size $2N_{fft} + 1N_{512}$. 44

4.9 Error performance of CP type detection in SUI4 channel at different speeds with window size $2N_{fft} + 1N_{512}$. 45

4.10 Error performance of CP type detection in Pedestrian-B channel at different speeds with window size $2N_{fft} + 1N_{512}$. 45

4.11 Pairs of data correlated with window size $6N_{fft} + 1N_{512}$. 46

4.12 Error performance of CP type detection in single-path channel at speed 3 km with several different window size. 47

4.13 Error performance of CP type detection in single-path channel at speed 120 km with several different window size. 47

4.14 Error performance of CP type detection in single-path channel at speed 360 km with several different window size. 48

4.15 Error performance of CP type detection in SUI1 channel at speed 3 km with several different window size. 48

4.16 Error performance of CP type detection in SUI1 channel at speed 120 km with several different window size. 49
4.17 Error performance of CP type detection in SUI1 channel at speed 360 km with several different window size. 49
4.18 Error performance of CP type detection in SUI2 channel at speed 3 km with several different window size. 50
4.19 Error performance of CP type detection in SUI2 channel at speed 120 km with several different window size. 50
4.20 Error performance of CP type detection in SUI2 channel at speed 360 km with several different window size. 51
4.21 Error performance of CP type detection in SUI3 channel at speed 3 km with several different window size. 51
4.22 Error performance of CP type detection in SUI3 channel at speed 120 km with several different window size. 52
4.23 Error performance of CP type detection in SUI3 channel at speed 360 km with several different window size. 52
4.24 Error performance of CP type detection in SUI4 channel at speed 3 km with several different window size. 53
4.25 Error performance of CP type detection in SUI4 channel at speed 120 km with several different window size. 53
4.26 Error performance of CP type detection in SUI4 channel at speed 360 km with several different window size. 54
4.27 Error performance of CP type detection in Pedestrian-B channel at speed 3 km with several different window size. 54
4.28 Error performance of CP type detection in Pedestrian-B channel at speed 120 km with several different window size. 55
4.29 Error performance of CP type detection in Pedestrian-B channel at speed 360 km with several different window size. 55

List of Tables

2.1 LTE System Attributes [2, Table 1.1] 6

2.2 Resource Block Parameters (modified from [1, Table 5.2.3-1]) 9

2.3 Physical Layer Cell Identities [2, Table 9.1] 13

2.4 Mapping Between $N_{ID}^{(1)}$ and Indices m_0 and m_1 [2, Table 9.2] 14

3.1 Joint Estimation of STO, CFO for Extended CP 34

3.2 Joint Estimation of STO, CFO for Normal CP 35

4.1 Downlink System Parameters Used in Simulation 37

4.2 SUI Channel Models for Three Terrain Types 37

4.3 SUI-1 Channel Model 37

4.4 SUI-2 Channel Model 38

4.5 SUI-3 Channel Model 38

4.6 SUI-4 Channel Model 38

4.7 PB Channel Model 39

Chapter 1

Introduction

Orthogonal frequency division multiple access (OFDMA) is the scheme chosen for the downlink of the 3rd Generation Partnership Project (3GPP) Long Term Evolution (LTE) and LTE-Advanced (LTE-A) standards for 4G cellular mobile communication [2].

When an user equipment (UE) is turned on or performs handoff from one cell to another, a first thing to do is synchronization, which includes OFDM symbol timing recovery (necessitated by the unknown propagation delay), carrier frequency recovery (necessitated by the mismatch of oscillators between the base station and the UE), detection of the cyclic prefix (CP) type used in signal transmission, and detection of the cell identity (cell ID) carried on the synchronization signals.

Various algorithms have been proposed to estimate symbol timing offset and carrier frequency offset and they can be classified into two main categories: data-aided estimation and nondata-aided (blind) estimation. In [6] and [9], the authors derive algorithms based on the maximum likelihood (ML) criterion for blind synchronization over an additive white Gaussian noise (AWGN) channel and single-path Rayleigh channel, respectively. In [10], the authors propose a technique to jointly estimate the symbol timing offset and carrier frequency offset over fast time-varying multipath channels. A pilot-aided method (using primary synchronization sequence) based on the ML approach that takes the unknown channel response into account is proposed in [11].

In our study, we consider blind synchronization and focus on LTE and LTE-A initial downlink synchronization estimation schemes based on the 3GPP TS 36.211 release 11 [1], including problem formulation, algorithm derivation based on the ML criterion and computer simulation in MATLAB.

The contribution of this work is as follows.

- We establish the transmitted and received signal models of LTE-A system and derive the quasi-maximum-likelihood estimator for joint estimation of the cyclic prefix (CP) type, symbol timing offset (STO) and carrier frequency offset (CFO).
- It is a generalized solution compared to that proposed in [6], [9] and [10]. The first and the second are considered in AWGN and single-path Rayleigh fading channels, respectively. The last is not an optimal ML estimator due to improper derivation. Our solution is derived based on the multipath fading channels.
- In estimating CFO, we consider an approximation so that it can reduce complexity largely. Though, by doing so, the solution is not optimal under multipath fading channels. It is an optimal solution under AWGN and single-path Rayleigh fading channels because the approximate term has no effect on estimation process.

This thesis is organized as follows.

- In chapter 2, we introduce the basic concepts of OFDMA and the LTE (LTE-A) downlink transmission standard based on the 3GPP TS 36.211 release 11 [1].
- In chapter 3, we first formulate our problem into mathematical model and then use the ML criterion to jointly estimate STO, CFO, and CP type.
- In chapter 4, we show some simulation results under different environments, and discuss the simulation results.
- In chapter 5, we give the conclusion about our proposed estimator and indicate some items of potential future work.

Chapter 2

Overview of the LTE-A Downlink Standard

The LTE-A downlink transmission standard is based on orthogonal frequency-division multiple access (OFDMA), a variant of orthogonal frequency-division multiplexing (OFDM). In this chapter, we first introduce the basic concepts of OFDM and OFDMA, then we give an overview of the LTE-A downlink specifications [1].

2.1 OFDM and OFDMA Basics

The material in this section is mainly taken from [2] and [3].

OFDM is a most popular scheme for current wireless systems, including 4G broadband wireless networks. The basic principle of OFDM is to derive the available spectrum into narrow-band parallel channels referred to as subcarriers so as to simplify channel equalization.

2.1.1 Discrete-time baseband OFDM system model

Fig. 2.1 shows the basic concept of baseband OFDM transmitter and receiver. In the transmitter side, the complex modulations symbols $X(k),\ k = 0, 1, ..., N-1$, are mapped to the input of inverse fast fourier transform (IFFT), and there is no information carried on the guard subcarriers. A cyclic prefix (CP) is added after IFFT operation and the resulting sequence is up-converted to RF for transmitting. In the receiver side, the received signal is filtered, amplified and down-converted from RF. Then the CP samples are removed and the received sample sequence are sent into the FFT. The discrete-time baseband channel is

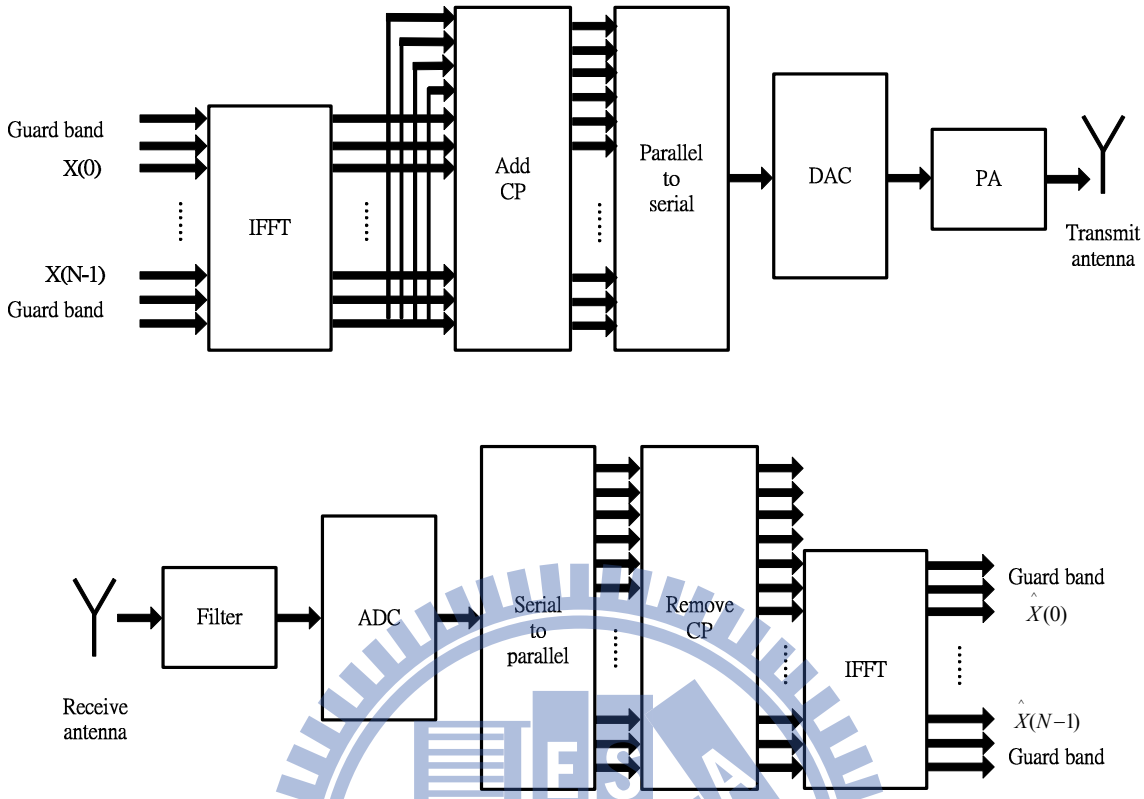

Figure 2.1: Baseband OFDM transmitter and receiver.

assumed to consist of L multipaths with tap coefficients $h_0, h_1, \cdots, h_{L-1}$, and the received signal after CP removal is given in the frequency domain by

$$\mathbf{Y} = \mathbf{HX} + \mathbf{z}, \tag{2.1}$$

where $\mathbf{H} = \text{diag}(H(0), H(1), \cdots, H(N-1))$ is the diagonal matrix of channel frequency response, and $\mathbf{z}$ is a vector of the additive white Gaussian noise (AWGN) with each element distributed according to $\mathcal{N}(0, \sigma_z^2)$.

2.1.2 Cyclic prefix

In OFDM systems, CP is used to overcome the inter-symbol interference (ISI) problem. We usually assume that the CP is longer than the length of the channel impulse response (CIR). Under this condition, successive OFDM symbols do not interfere with each other in the frequency domain if the receiver has proper time and frequency synchronization.

CP extends the OFDM symbol length by copying the last samples of the OFDM symbol into its front. In Fig. 2.2, T_G denotes the length of CP in terms of samples. After adding

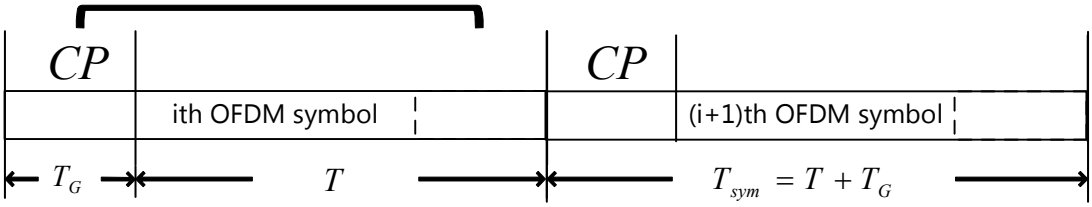

Figure 2.2: OFDM symbols with CP.

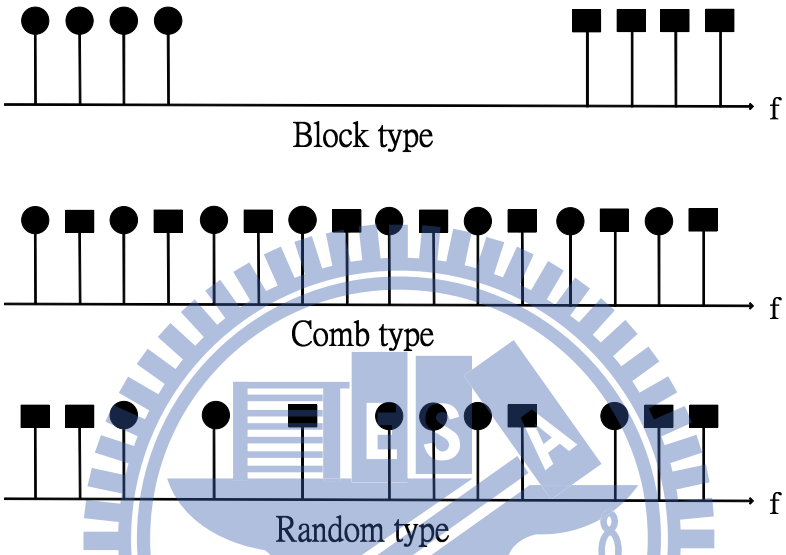

Figure 2.3: Types of resource allocation in OFDMA system (modified from [3, Fig. 4.29]).

CP, the OFDM symbol now has the duration $T_{sym} = T + T_G$.

2.1.3 OFDMA

In principle, in OFDM, all subcarriers in a symbol are used for transmitting the signal of a single device. OFDMA may share the subcarriers of a symbol among multiple devices or users. In practice, the multiple devices/users are allocated mutually exclusive sets of orthogonal subcarriers, so that the data of different devices/users can be separated in the frequency domain. One typical structure is subchannel OFDMA. A subset of subcarriers is allocated to each user by different types such as block type, comb type or random type. In the first type, each subchannel consists of a set of adjacent subcarriers. In the second type, each subchannel is composed of equi-spaced subcarriers. And in the last, each subchannel is composed of a set of subcarriers distributed randomly over the whole frequency band. Fig. 2.3 shows the three types of resource allocation in an OFDMA system.

Table 2.1: LTE System Attributes [2, Table 1.1]

Bandwidth	1.25–20 MHz	
Duplexing	FDD, TDD, half-duplex FDD	
Mobility	350km/h	
Multiple access	downlink	OFDMA
	Uplink	Single-carrier-FDMA
Multi-input multi-output (MIMO) modes	downlink	$2 \times 2, 4 \times 2, 4 \times 4$
	Uplink	$1 \times 2, 1 \times 4$
MIMO data rates	downlink	173 and 326 Mb/s for 2×2 and 4×4 MIMO, respectively
	Uplink	86 Mb/s with 1×2 antenna configuration
Modulation	QPSK, 16-QAM and 64-QAM	
Channel coding	Turbo code	
Other techniques	Channel sensitive scheduling, link adaptation, power control, inter-cell interference coordination (ICIC) and hybrid ARQ	

2.2 Overview of LTE and LTE-A Downlink Specifications

The contents in this section are mainly taken from [1] and [2].

The goal of LTE is to provide a high-data-rate, low-latency and packet-optimized radio access technology supporting flexible bandwidth deployments. In parallel, new network architecture is designed with the goal to support packet-switched traffic with seamless mobility, quality of service and minimal latency.

The air-interface related attributes of the LTE system are summarized in Table 2.1. The system supports flexible bandwidths. In addition to frequency division duplexing (FDD) and time division duplexing (TDD), half-duplex FDD is allowed to support low cost user equipment (UE). Unlike FDD, in half-duplex FDD operation a UE is not required to transmit and receive at the same time. This avoids the need for a costly duplexer in the UE. The system is primarily optimized for low speeds up to 15 km/h. However, the system specifications allow mobility support in excess of 350 km/h with some performance degradation.

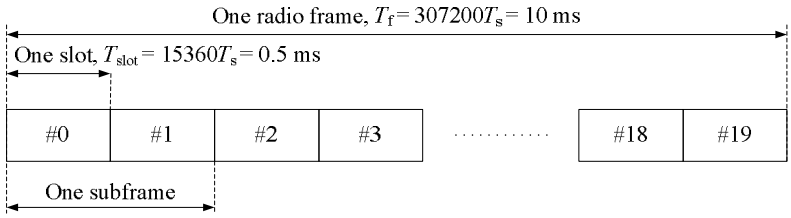

Figure 2.4: Frame structure type 1 [1, Fig.4.1-1].

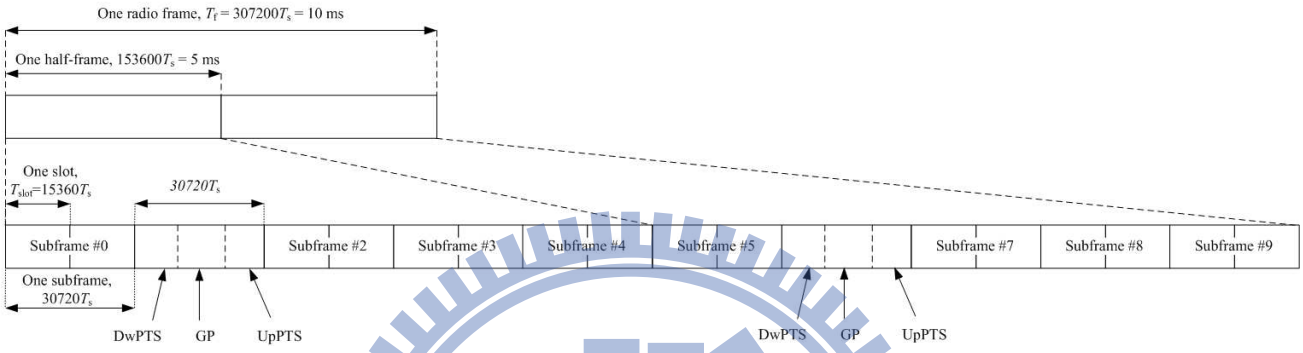

Figure 2.5: Frame structure type 2 [1, Fig. 4.2-1].

2.2.1 Frame structure

In the specification of the frame structure in LTE, the size in the time domain is normally expressed in time units of $T_s = 1/(15000 \times 2048)$ seconds. Both downlink and uplink transmissions are organized into radio frames with frame duration $T_f = 307200 \times T_s = 10$ ms. Fig. 2.4 and 2.5 show frame structure types 1 and 2, respectively. Frame structure type 1 applies to both full duplex and half duplex FDD, and frame structure type 2 applies to TDD. In our study, we focus on frame structure type 1. In this type, each radio frame consists of 20 slots of length $T_{slot} = 15360 \times T_s = 0.5$ ms, which are numbered from 0 to 19. A subframe consists of two consecutive slots where subframe i consists of slots $2i$ and $2i + 1$. For FDD, there are 10 subframes for downlink and uplink transmissions in each 10 ms interval.

2.2.2 Slot structure and physical resources

In LTE-A specifications, two CP lengths, called normal CP and extended CP, are defined to support small and large cells deployments, respectively. Fig. 2.6 shows the high-level slot structures for normal and extended CP and Fig. 2.7 shows the detailed slot structure for the

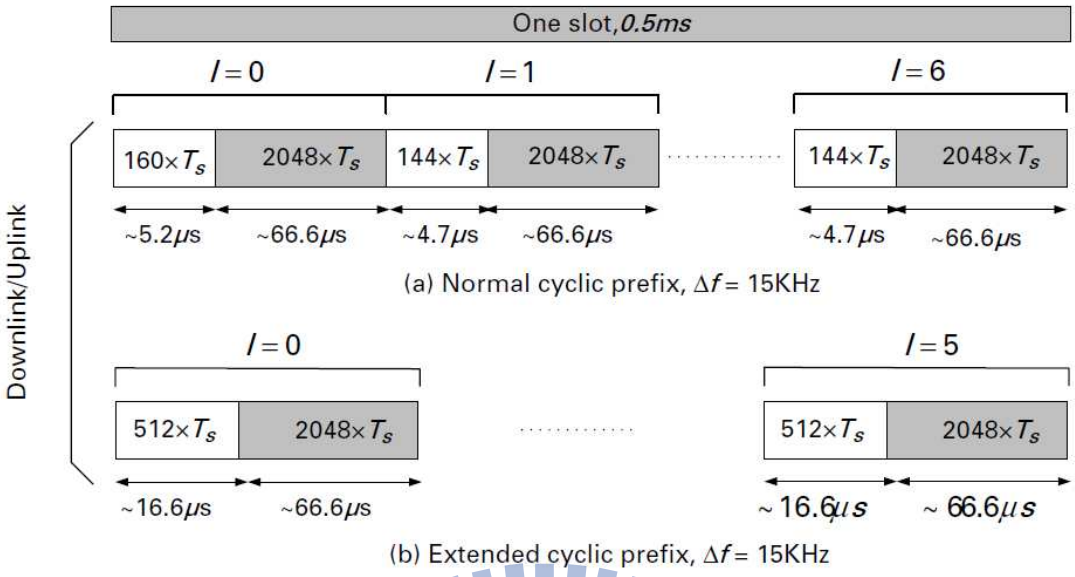

Figure 2.6: Slot structure for normal and extended CP [2, Fig. 8.3].

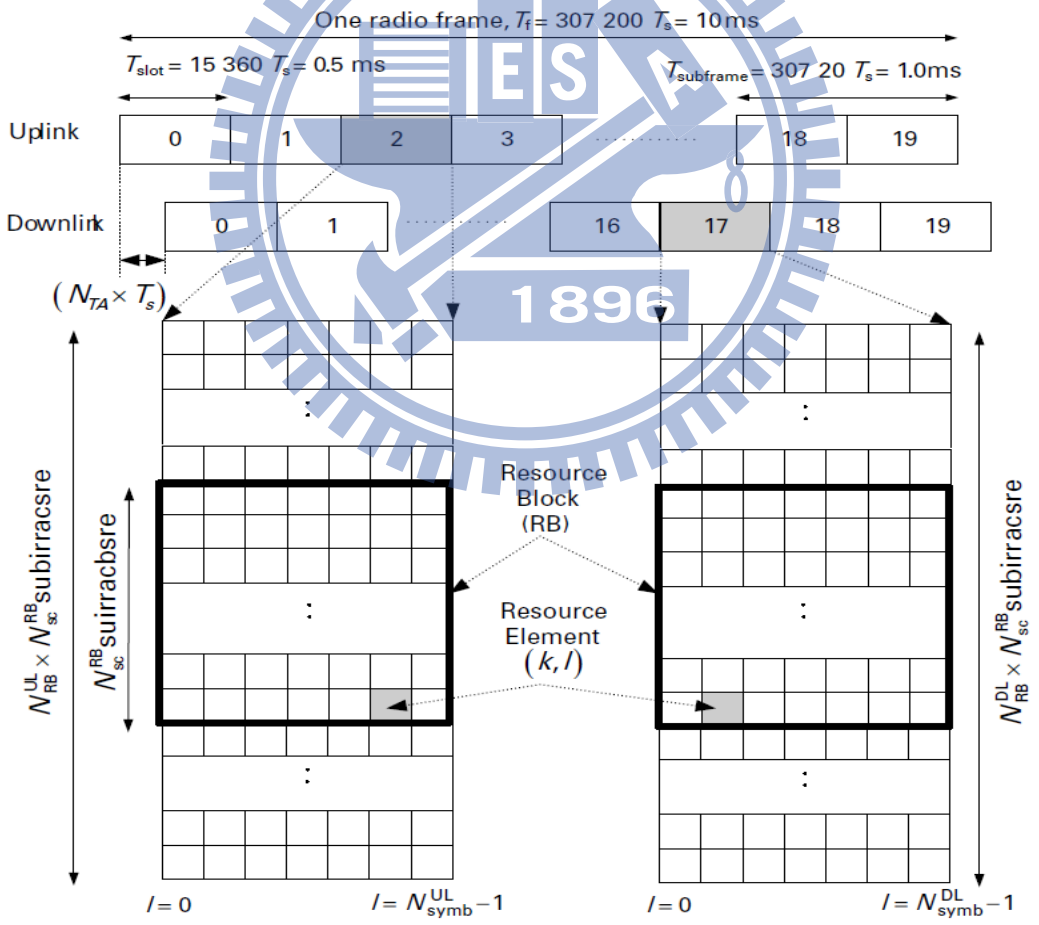

Figure 2.7: Detailed signal structure for normal CP [1, Figs. 5.2.1-1 and 6.2.2-1], [2, Fig. 8.2].

Table 2.2: Resource Block Parameters (modified from [1, Table 5.2.3-1])

Configuration	N_{sc}^{RB}	N_{symb}^{DL}	N_{symb}^{UL}
Normal CP	12	7	7
Extended CP	12	6	6
	24	3	NA

case of normal CP. The normal CP length is 5.2 μs ($160 \times T_s$) in the first OFDMA symbol and 4.7 μs ($144 \times T_s$) in the remaining six symbols. In the type of extended CP, the CP length is 16.6 μs ($512 \times T_s$) is the same in all the six symbols. The same applies to SC-FDMA symbols in the uplink.

A resource block (RB) is defined as N_{sc}^{RB} consecutive subcarriers in the frequency domain and N_{symb}^{DL} OFDMA symbols for the downlink or N_{symb}^{UL} SC-FDMA symbols for the uplink. An RB therefore consists of $N_{symb}^{DL} \times N_{sc}^{RB}$ ($N_{symb}^{UL} \times N_{sc}^{RB}$) resource elements (REs) in the downlink (uplink), which corresponds to one slot in the time domain and 180 kHz bandwidth in the frequency domain. The number of subcarriers within an RB N_{SC}^{RB} is 12 or 24 for the case of 15 kHz or 7.5 kHz subcarrier spacing, respectively. Table 2.2 summarizes the parameter sets.

The minimum and maximum number of RBs in a slot are 6 (1.08 MHz transmission bandwidth) and 110 (19.8 MHz transmission bandwidth), respectively. The relation between the RB number (or index) n_{RB} in the frequency domain and RE index (k, l) in a slot is given by

$$n_{RB} = \lfloor \frac{k}{N_{sc}^{RB}} \rfloor.$$

2.2.3 Random access

Fig. 2.8 shows the random access procedure. When a UE is turned on or performs handoff from one cell to another, the first thing to do is to acquire timing and frequency synchronization. This procedure is achieved by using the received primary synchronization sequences (PSS), secondary synchronization sequences (SSS) and the broadcast channel (BCH). After synchronization and getting system information including random access (RA) parameters, the UE can then transmit the RA preamble. The purpose of RA is to let the base station (eNB in LTE terminology) estimate and adjust the UE uplink transmission timing to within a fraction of the CP. When the eNB receives an RA preamble successfully, it sends the

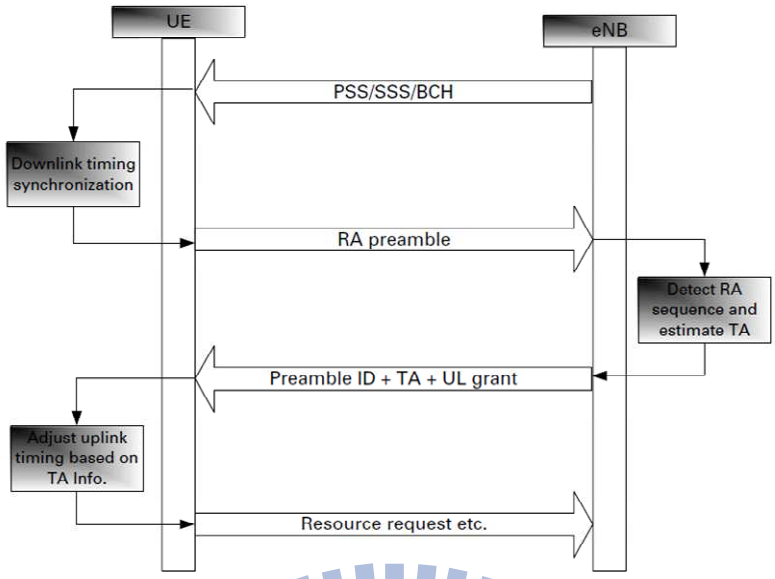

Figure 2.8: Random access procedure [2, Figure 10.1].

response sequence indicating the successfully received preamble, timing advance (TA) and information about uplink resource allocation to the UE.

The UE determines if its RA preamble has been successfully received by matching the preamble number with that received from the eNB. If they match, the UE uses the TA information to adjust its uplink timing, sends uplink scheduling or a resource request indicated in the RA response message.

2.2.4 Cell search

Besides timing and frequency synchronization, when a UE turns on or performs handoff from one cell to another, it also should detect the cell identity (cell ID), transmission bandwidth of the system, CP type, and numbers of transmit antenna ports, etc. This procedure is achieved by using the PSS, SSS, and BCH. To facilitate such work, the PSS, SSS and BCH are transmitted using the same minimum bandwidth of 1.08 MHz in the central part of the bandwidth. PSS and SSS are carried in the last and second last OFDM symbols respectively in slot numbers 0 and 10, and in the frequency domain over the middle 62 subcarriers out of a total of 72 subcarriers (1.08 MHz). Fig. 2.9 shows the position of PSS and SSS under normal CP.

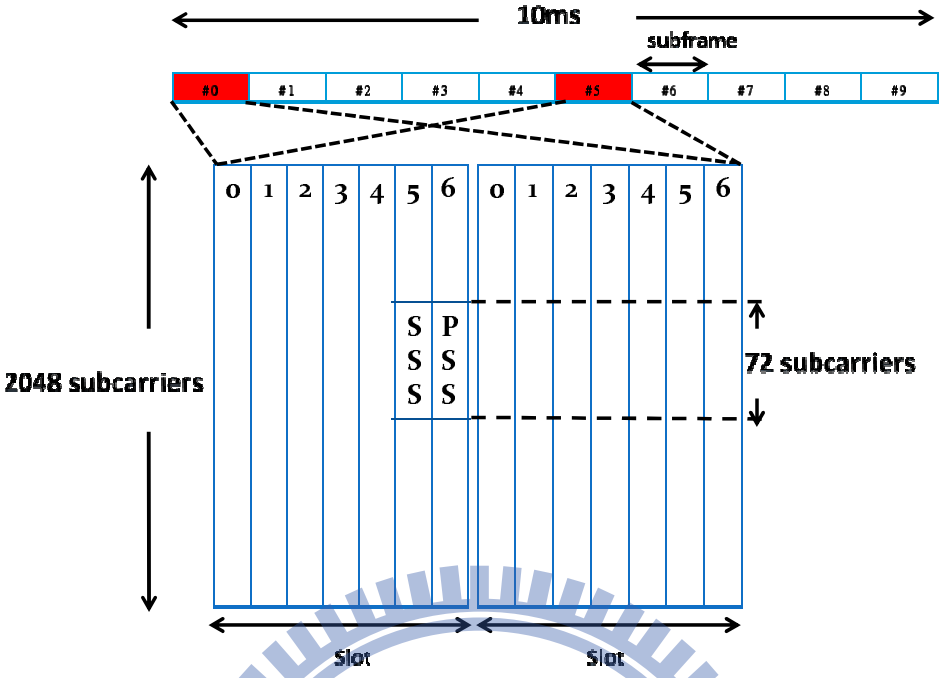

Figure 2.9: downlink frame structure for the type of normal CP.

2.2.5 Zadoff-Chu (ZC) sequences

A ZC sequence is defined as

$$x_u(m) = \begin{cases} e^{-j\frac{\pi u m^2}{N_{ZC}}}, & \text{when } N_{ZC} \text{ is even,} \\ e^{-j\frac{\pi u m(m+1)}{N_{ZC}}}, & \text{when } N_{ZC} \text{ is odd,} \end{cases} \tag{2.2}$$

with $m = 0, 1, ..., N_{ZC} - 1$, and the sequence index u is relatively prime to the length of ZC sequence N_{ZC}.

ZC sequences are used in many sequences in the LTE system such as PSS, uplink reference signals, uplink physical control channel (PUCCH) and RA channel. Some properties of the ZC sequences are as follows. First, the periodic autocorrelation of a ZC sequence is zero for all time shifts other than zero. Second, ZC sequences for different u exhibit low cross-correlation, though are not orthogonal. And third, if the sequence length N_{ZC} is a prime number, then there are $(N_{ZC} - 1)$ different sequences with periodic cross-correlation of $1/\sqrt{N_{ZC}}$ between any two sequences regardless of time shift.

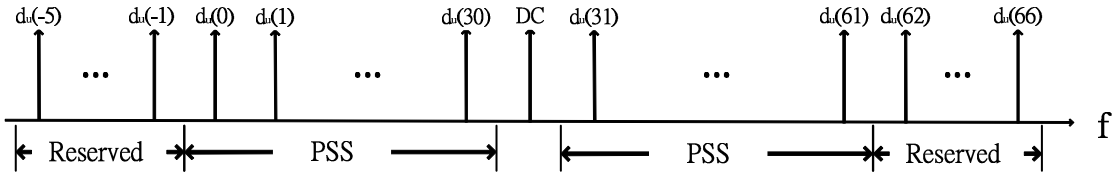

Figure 2.10: PSS mapping in the frequency domain (modified from [2, Figure 9.4]).

2.2.6 Primary synchronization signal (PSS)

In the LTE system, a total of 504 unique physical layer cell IDs are provided. It is derived from a physical layer cell ID index $N_{ID}^{(1)} \in [0, 167]$ and another physical layer ID $N_{ID}^{(2)} \in [0, 2]$, where $N_{ID}^{(1)}$ and $N_{ID}^{(2)}$ are integers. The cell ID is defined to be $N_{ID}^{(cell)} = 3N_{ID}^{(1)} + N_{ID}^{(2)}$.

The PSS in the frequency domain is defined as

$$d_u(n) = \begin{cases} e^{-j\frac{\pi un(n+1)}{63}}, & n = 0, 1, ..., 30, \\ e^{-j\frac{\pi un(n+1)(n+2)}{63}}, & n = 31, 32, ..., 61, \end{cases} \tag{2.3}$$

where the ZC root sequence index u is 25, 29, and 34 for $N_{ID}^{(2)} = 0, 1$, and 2, respectively.

The mapping of the PSS sequence $d_u(n)$ to the REs is as shown in Fig. 2.10. The mapping for the non-reserved REs is as follows:

$$a_{k,l} = d_u(n), \ k = n - 31 + \lfloor \frac{N_{RB}^{DL} N_{sc}^{RB}}{2} \rfloor, \ l = N_{symb}^{DL} - 1, \ n = 0, ..., 61. \tag{2.4}$$

The signal values of the reserved REs are set to null, i.e., for $k = n - 31 + \lfloor \frac{N_{RB}^{DL} N_{sc}^{RB}}{2} \rfloor$, $l = N_{symb}^{DL} - 1$, $n = -5, -4, ..., -1, 62, 63, ..., 66$.

2.2.7 Secondary synchronization signal (SSS)

The sequence of SSS is an interleaved concatenation of the two length-31 binary sequences. The concatenated sequence is scrambled with the sequence of PSS. The combination of two length-31 sequences defining the SSS differs between subframes 0 and 5, and is defined as

$$d(2n) = \begin{cases} s_0^{(m_0)}(n)c_0(n), & \text{in subframe 0}, \\ s_1^{(m_1)}(n)c_0(n), & \text{in subframe 5}, \end{cases} \tag{2.5}$$

$$d(2n+1) = \begin{cases} s_1^{(m_1)}(n)c_1(n)z_1^{(m_0)}(n), & \text{in subframe 0}, \\ s_0^{(m_0)}(n)c_1(n)z_1^{(m_1)}(n), & \text{in subframe 5}, \end{cases} \tag{2.6}$$

Table 2.3: Physical Layer Cell Identities [2, Table 9.1]

PHY layer cell ID group $N_{ID}^{(1)}$	PHY layer ID $N_{ID}^{(2)}$	PHY layer cell ID $N_{ID}^{(cell)} = 3N_{ID}^{(1)} + N_{ID}^{(2)}$
	0	0
0	1	1
	2	2
	0	3
1	1	4
	2	5
⋮	⋮	⋮
	0	501
167	1	502
	2	503

where $0 \leq n \leq 30$. The indices m_0 and m_1 are derived from $N_{ID}^{(1)}$ according to

$$\begin{aligned} m_0 &= m' \mod 31, \\ m_1 &= (m_0 + \lfloor m'/31 \rfloor + 1) \mod 31, \\ m' &= N_{ID}^{(1)} + q(q+1)/2, \; q = \lfloor \frac{N_{ID}^{(1)} + q'(q'+1)/2}{30} \rfloor, \; q' = \lfloor N_{ID}^{(1)}/30 \rfloor. \end{aligned} \tag{2.7}$$

The mapping between $N_{ID}^{(1)}$ and indices m_0 and m_1 is illustrated in Table 2.4.

The two sequences $s_0^{(m_0)}(n)$ and $s_1^{(m_1)}(n)$ are defined as two different cyclic shifts of the m-sequence $\tilde{s}(n)$ according to

$$\begin{aligned} s_0^{(m_0)}(n) &= \tilde{s}((n + m_0) \mod 31), \\ s_1^{(m_1)}(n) &= \tilde{s}((n + m_1) \mod 31), \end{aligned} \tag{2.8}$$

where $\tilde{s}(i) = 1 - 2x(i)$, $0 \leq i \leq 30$, with $x(i)$ given as

$$x(j+5) = (x(j+2) + x(j)) \mod 2, \; 0 \leq j \leq 25, \tag{2.9}$$

with initial conditions $x(0) = x(1) = x(2) = x(3) = 0, \; x(4) = 1$.

The two length-31 scrambling sequences $c_0(n)$ and $c_1(n)$ which are dependent on PSS are defined by two different cyclic shifts of the m-sequence $\tilde{c}(n)$ as

$$\begin{aligned} c_0(n) &= \tilde{c}((n + N_{ID}^{(2)}) \mod 31), \\ c_1(n) &= \tilde{c}((n + N_{ID}^{(2)} + 3) \mod 31), \end{aligned} \tag{2.10}$$

Table 2.4: Mapping Between $N_{ID}^{(1)}$ and Indices m_0 and m_1 [2, Table 9.2]

$N_{ID}^{(1)}$	m_0	m_1	$N_{ID}^{(1)}$	m_0	m_1
0	0	1	⋮	⋮	⋮
1	1	2	113	26	30
⋮	⋮	⋮	114	0	5
29	29	30	115	1	6
30	0	2	⋮	⋮	⋮
31	1	3	139	25	30
⋮	⋮	⋮	140	0	6
58	28	30	141	1	7
59	0	3	⋮	⋮	⋮
60	1	4	164	24	30
⋮	⋮	⋮	165	0	7
86	27	30	166	1	8
87	0	4	167	2	9
88	1	5			

where $\tilde{c}(i) = 1 - 2x(i)$, $0 \leq i \leq 30$, with $x(i)$ given as

$$x(j+5) = (x(j+3) + x(j)) \mod 2, \ 0 \leq j \leq 25, \tag{2.11}$$

with initial conditions $x(0) = x(1) = x(2) = x(3) = 0, \ x(4) = 1$.

The two length-31 scrambling sequences $z_1^{(m_0)}(n)$ and $z_1^{(m_1)}(n)$ are defined by a cyclic shift of the m-sequence $\tilde{z}(n)$ according to

$$\begin{aligned} z_1^{(m_0)}(n) &= \tilde{z}((n + (m_0 \mod 8)) \mod 31), \\ z_1^{(m_1)}(n) &= \tilde{z}((n + (m_1 \mod 8)) \mod 31), \end{aligned} \tag{2.12}$$

where $\tilde{z}(i) = 1 - 2x(i)$, $0 \leq i \leq 30$, with $x(i)$ given as

$$x(j+5) = (x(j+4) + x(j+2) + x(j+1) + x(j)) \mod 2, \ 0 \leq j \leq 25, \tag{2.13}$$

with initial conditions $x(0) = x(1) = x(2) = x(3) = 0, \ x(4) = 1$.

The SSS mapping for the non-reserved REs has the following relationship:

$$a_{k,l} = d_u(n), \ k = n - 31 + \lfloor \frac{N_{RB}^{DL} N_{sc}^{RB}}{2} \rfloor, \ l = N_{symb}^{DL} - 2, \ n = 0, ..., 61. \tag{2.14}$$

The signal values of the reserved REs are set to null, i.e., $k = n - 31 + \lfloor \frac{N_{RB}^{DL} N_{sc}^{RB}}{2} \rfloor$, $l = N_{symb}^{DL} - 2$, $n = -5, -4, ..., -1, 62, 63, ..., 66$. Fig. 2.11 shows the SSS mapping in the frequency domain.

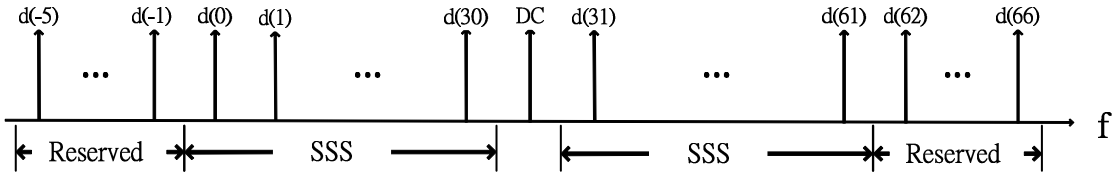

Figure 2.11: SSS mapping in the frequency domain (modified from [2, Figure 9.5]).

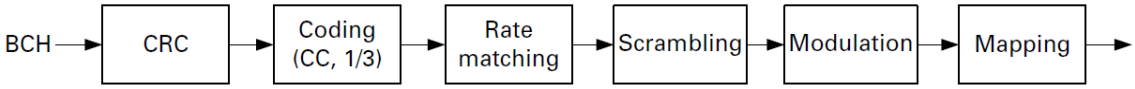

Figure 2.12: BCH transmission chain processing [2, Figure 9.6].

2.2.8 Broadcast channel (BCH)

Fig. 2.12 shows the transmission processing chain for the BCH. First, error detection capability is provided on BCH transport blocks through cyclic-redundancy-check (CRC) coding. After CRC attachment, the bit sequence is coded using a rate 1/3 tail-biting convolutional code. Then the bits are rate matched using a certain circular buffer approach to obtain the rate-matched sequence $b(0),\ b(1),\ \cdots, b(M_{bit}-1)$, where M_{bit} is the number of transmitted bits. And then the rate-matched sequence is scrambled with a cell-specific sequence as

$$\tilde{b}(i) = (b(i) + c(i)) \mod 2 \tag{2.15}$$

with frame number n_f fulfilling the condition

$$n_f \mod 4 = 0 \tag{2.16}$$

and

$$\begin{aligned} c(n) &= (x_1(n+N_c) + x_2(n+N_c)) \mod 2, \\ x_1(n+31) &= (x_1(n+3) + x_1(n)) \mod 2, \\ x_2(n+31) &= (x_2(n+3) + x_2(n+2) + x_2(n+1) + x_2(n)) \mod 2, \end{aligned} \tag{2.17}$$

where $N_c = 1600$, the m-sequence $x_1(n)$ is initialized with $x_1(0) = 1$, $x_1(n) = 0$, $n = 1, 2, ..., 30$, and the m-sequence $x_2(n)$ is initialized by $c_{init} = \sum_{i=0}^{30} x_2(i) \times 2^i$ with the value depending on the application of the sequence.

Fig. 2.13 shows the mapping of the physical BCH. It is transmitted over 4 subframes with a 40 ms timing interval. The number of subcarriers used for PBCH is 72 in the third

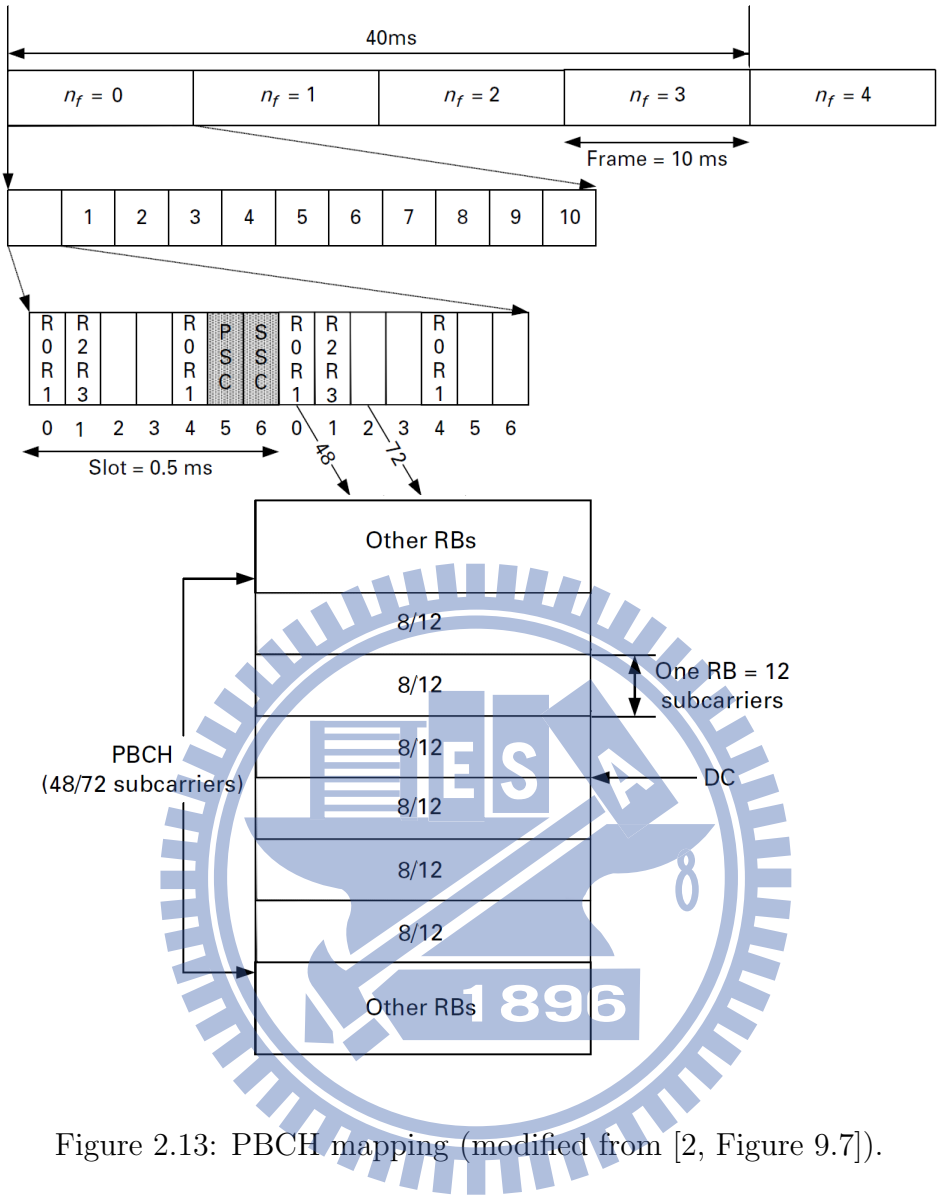

Figure 2.13: PBCH mapping (modified from [2, Figure 9.7]).

and fourth OFDMA symbols in the slot without reference signals and is 48 in the first and second OFDMA symbols with reference signals.

Chapter 3

Initial Downlink Synchronization

In this chapter, we first formulate the the initial downlink synchronization problem for the 4G LTE-A FDD system. Then we derive a solution algorithm by taking a maximum likelihood (ML) approach.

3.1 The Initial Downlink Synchronization Problem

When an user equipment (UE) tries to gain connection with a base station (eNB), the UE first needs to synchronize to the eNB. In so doing, it first has to estimate the symbol timing offset (STO), carrier frequency offset (CFO), and the cyclic prefix (CP) type. The STO can arise from the unknown propagation delay between the transmitter and receiver, and the CFO from the mismatch between transmitter and receiver oscillators and the Doppler spread due to mobility. As to the CP type, recall that the LTE-A system defines two CP lengths, namely normal CP and extended CP, to support small and large cells deployments respectively. Hence the UE also has to detect the CP type for signal reception as well as transmission.

3.1.1 Transmission system model

The overall system structure is shown in Figure 3.1. Figure 3.2 depicts the slot structure in the time domain that captures the essence.

Let $m = 1$ and $m = 2$ represent extended CP and normal CP, respectively. Let $\mathbf{d}_m^i(j)$ donote the frequency domain signal vector transmitted in the jth OFDMA symbol of the ith slot under CP type m. The size of $\mathbf{d}_m^i(j)$ is N, the FFT size used by the system. Let $\mathbf{s}_m^i$

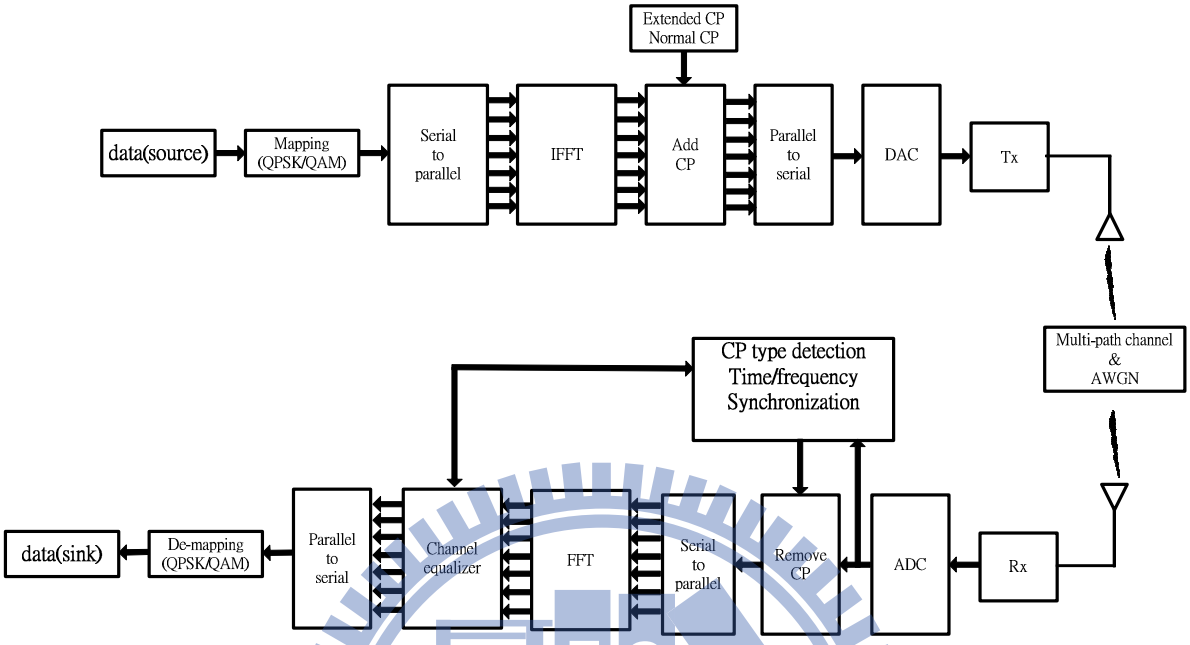

Figure 3.1: Transmission system structure.

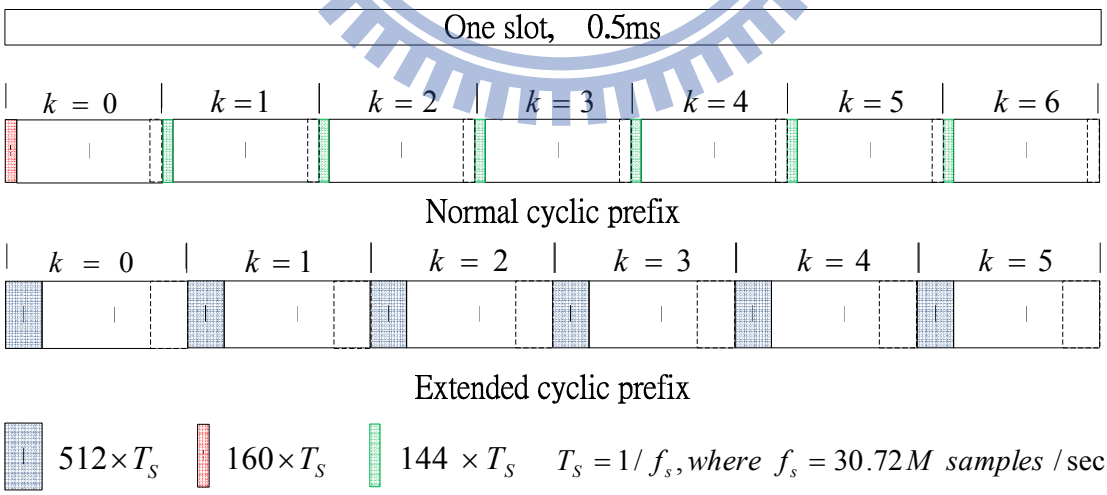

Figure 3.2: Slot structure in the time domain.

be a collection of the signal vectors in each slot as

$$\mathbf{s}_m^i = \begin{cases} [\mathbf{d}_1^i(0)\ \mathbf{d}_1^i(1)\ \cdots\ \mathbf{d}_1^i(5)]^T, & m=1, \\ [\mathbf{d}_2^i(0)\ \mathbf{d}_2^i(1)\ \cdots\ \mathbf{d}_2^i(6)]^T, & m=2. \end{cases} \tag{3.1}$$

The baseband transmitted signal can be written as

$$\mathbf{x}_m^i = \mathbf{G}_m \cdot \mathbf{F}_m^H \cdot \mathbf{s}_m^i \tag{3.2}$$

where $\mathbf{F}_m$ is as $N_m \times N_m$ block diagonal matrix given by

$$\mathbf{F}_m = \begin{cases} \text{diag}(\mathbf{F},\ \mathbf{F},\ \mathbf{F},\ \mathbf{F},\ \mathbf{F},\ \mathbf{F}), & m=1, \\ \text{diag}(\mathbf{F},\ \mathbf{F},\ \mathbf{F},\ \mathbf{F},\ \mathbf{F},\ \mathbf{F},\ \mathbf{F}), & m=2, \end{cases} \tag{3.3}$$

with $N_1 = 6N$, $N_2 = 7N$ and $\mathbf{F}$ being the normalized $N \times N$ DFT matrix given by

$$\mathbf{F} = \frac{1}{\sqrt{N}} \begin{bmatrix} \omega_N^{0\cdot 0} & \omega_N^{0\cdot 1} & \cdots & \omega_N^{0\cdot(N-1)} \\ \omega_N^{1\cdot 0} & \omega_N^{1\cdot 1} & \cdots & \omega_N^{1\cdot(N-1)} \\ \vdots & \vdots & \ddots & \vdots \\ \omega_N^{(N-1)\cdot 0} & \omega_N^{(N-1)\cdot 1} & \cdots & \omega_N^{(N-1)\cdot(N-1)} \end{bmatrix} \tag{3.4}$$

where $\omega_N = e^{-j2\pi\frac{1}{N}}$; $\mathbf{G}_m$ is the CP insert matrix given by

$$\mathbf{G}_1 = \begin{bmatrix} \mathbf{G}_{CP1} & \mathbf{0} & \cdots & \cdots & \cdots & \mathbf{0} \\ \mathbf{0} & \mathbf{G}_{CP1} & \mathbf{0} & \ddots & \ddots & \mathbf{0} \\ \mathbf{0} & \mathbf{0} & \mathbf{G}_{CP1} & \mathbf{0} & \ddots & \mathbf{0} \\ \mathbf{0} & \ddots & \mathbf{0} & \mathbf{G}_{CP1} & \mathbf{0} & \mathbf{0} \\ \mathbf{0} & \ddots & \ddots & \mathbf{0} & \mathbf{G}_{CP1} & 0 \\ \mathbf{0} & \cdots & \cdots & \cdots & \mathbf{0} & \mathbf{G}_{CP1} \end{bmatrix} \tag{3.5}$$

with

$$\mathbf{G}_{CP1} = \begin{bmatrix} \mathbf{0}_{N_{512}\times(N-N_{512})} & \mathbf{I}_{N_{512}} \\ \mathbf{I}_{(N-N_{512})} & \mathbf{0} \\ \mathbf{0} & \mathbf{I}_{N_{512}} \end{bmatrix}, \tag{3.6}$$

$$\mathbf{G}_2 = \begin{bmatrix} \mathbf{G}_{CP2} & \mathbf{0} & \cdots & \cdots & \cdots & \cdots & \mathbf{0} \\ \mathbf{0} & \mathbf{G}_{CP3} & \mathbf{0} & \ddots & \ddots & \ddots & \mathbf{0} \\ \mathbf{0} & \mathbf{0} & \mathbf{G}_{CP3} & \mathbf{0} & \ddots & \ddots & \mathbf{0} \\ \mathbf{0} & \ddots & \mathbf{0} & \mathbf{G}_{CP3} & \mathbf{0} & \ddots & \mathbf{0} \\ \mathbf{0} & \ddots & \ddots & \mathbf{0} & \mathbf{G}_{CP3} & \mathbf{0} & \mathbf{0} \\ \mathbf{0} & \cdots & \cdots & \cdots & \mathbf{0} & \mathbf{G}_{CP3} & \mathbf{0} \\ \mathbf{0} & \cdots & \cdots & \cdots & \cdots & \mathbf{0} & \mathbf{G}_{CP3} \end{bmatrix} \tag{3.7}$$

with

$$\mathbf{G}_{CP2} = \begin{bmatrix} \mathbf{0}_{N_{160}\times(N-N_{160})} & \mathbf{I}_{N_{160}} \\ \mathbf{I}_{(N-N_{160})} & \mathbf{0} \\ \mathbf{0} & \mathbf{I}_{N_{160}} \end{bmatrix},\ \mathbf{G}_{CP3} = \begin{bmatrix} \mathbf{0}_{512\times(N-N_{512})} & \mathbf{I}_{N_{144}} \\ \mathbf{I}_{(N-N_{144})} & \mathbf{0} \\ \mathbf{0} & \mathbf{I}_{N_{144}} \end{bmatrix}, \tag{3.8}$$

where N_{512}, N_{160}, N_{144} are the CP lengths of different OFDMA symbols under different CP type as shown in Figure 3.2.

The above gives the signal structure in a slot, we can concatenate the slots together to obtain the overall transmitted signal. For this, we define the rectangular window matrix $\mathbf{W}_i \in \mathbf{R}^{\infty \times M}$ for the ith slot as

$$\mathbf{W}_i = \mathbf{e}_i \otimes \mathbf{I}_M, \tag{3.9}$$

where $\otimes$ is the Kronecker product operation. Then the infinite-length transmitted signal can be written as

$$\mathbf{y} = \sum_{i=-\infty}^{\infty} \mathbf{W}_i \cdot \mathbf{x}_m^i. \tag{3.10}$$

At the receiver, let the observation window size be K samples. Then the observed received signal $\mathbf{r} \in \mathbf{C}^{K\times 1}$ suffers from the influence of the multi-path channel and the effect of the carrier frequency offset and symbol timing offset. It can be modeled as

$$\mathbf{r} = \mathbf{D}(\theta) \cdot \mathbf{A}(\epsilon) \cdot \mathbf{H} \cdot \mathbf{y} + \mathbf{w}, \tag{3.11}$$

where $\mathbf{w}$ is the additive white Gaussian noise (AWGN) vector with zero mean and variance σ_w^2, $\mathbf{A}(\epsilon) \in \mathbf{C}^{\infty\times\infty}$ is the CFO matrix with the (p,q)th element given by

$$[\mathbf{A}(\epsilon)]_{p,q} = e^{j2\pi p\epsilon/N}\delta(p-q), \tag{3.12}$$

$\mathbf{D}(\theta) \in \mathbf{R}^{K\times\infty}$ is the STO matrix, which means collecting K samples from the overall signal, and its (p,q)th element is given by

$$[\mathbf{D}(\theta)]_{p,q} = \delta(q-p-\theta), \tag{3.13}$$

$\mathbf{H} \in \mathbf{C}^{\infty\times\infty}$ is the channel impulse response matrix given by

$$\mathbf{H} = \begin{bmatrix} \ddots & \ddots & \ddots & \ddots & \ddots & \ddots & \ddots & \ddots & \ddots & \ddots \\ \ddots & 0 & h(N_g-1,0) & \cdots & \cdots & h(0,0) & 0 & \ddots & \ddots & \ddots \\ \ddots & \ddots & 0 & h(N_g-1,1) & \cdots & \cdots & h(0,1) & 0 & \ddots & \ddots \\ \ddots & \ddots & \ddots & 0 & h(N_g-1,2) & \cdots & \cdots & h(0,2) & 0 & \ddots \\ \ddots & \ddots & \ddots & \ddots & \ddots & \ddots & \ddots & \ddots & \ddots & \ddots \end{bmatrix}, \tag{3.14}$$

where the (p,q)th element is given by

$$[\mathbf{H}]_{p,q} = h(l,n)|_{0\le l=p-q\le N_g-1, n=p}, \tag{3.15}$$

with l and n being the delay and time indices. We have assumed that the channel impulse response (CIR) length is smaller than the CP length in order to avoid the inter-symbol-interference (ISI) problem, so $h(l,n)$ is nonzero only when $0 \le l \le N_g - 1$ and $N_g = N_{144}$.

3.1.2 The ML approach to synchronization

Eq. (3.15) gives the received signals. We take the ML approach to estimate the parameters θ, ϵ and m, i.e., the STO, CFO and CP type, which give the ML estimation as

$$\begin{aligned} \{\hat{\theta}, \hat{\epsilon}, \hat{m}\} &= \max_{\theta,\epsilon,m} f(\mathbf{r}|\theta, \epsilon, m) \\ &= \max_{m} \max_{\theta,\epsilon|m} f(\mathbf{r}|\theta, \epsilon, m) \end{aligned} \tag{3.16}$$

where $f(\mathbf{r}|\theta, \epsilon, m)$ is the likelihood function.

Therefore, the two key issues are the derivation of the likelihood function and the solution of the ML estimation problem. We first derive the likelihood function for extended CP. Then we consider the normal CP case. And finally we derive the solution.

3.2 Solution of the ML Estimation Problem

3.2.1 Derivation of the likelihood function for extended CP

The likelihood function for extended CP is given by

$$p(\mathbf{r}|\theta_1, \epsilon_1, m = 1) = \frac{\exp(-\mathbf{r}^H \cdot \mathbf{C}_r^{-1} \cdot \mathbf{r})}{\pi^K \cdot \det(\mathbf{C}_r)} \tag{3.17}$$

where $\mathbf{C}_r$ is the autocorrelation matrix of the received signals $\mathbf{r}$ given by (3.11). To derive $\mathbf{C}_r$, consider first the autocorrelation matrix of the transmitted signal $\mathbf{y}$ given by

$$\mathbf{C}_y = E\{\mathbf{y} \cdot \mathbf{y}^H\} \tag{3.18}$$

$$= E\{(\sum_{i=-\infty}^{\infty} \mathbf{W}_i \cdot \mathbf{x}_1^i) \cdot (\sum_{j=-\infty}^{\infty} \mathbf{W}_j \cdot \mathbf{x}_1^j)^H\} \tag{3.19}$$

$$= \sum_{i=-\infty}^{\infty} \sum_{j=-\infty}^{\infty} \mathbf{W}_i \cdot \mathbf{G}_1 \cdot \mathbf{F}_1^H \cdot E\{\mathbf{s}_1^i \cdot (\mathbf{s}_1^j)^H\} \cdot \mathbf{F}_1 \cdot \mathbf{G}_1^H \cdot \mathbf{W}_j^H \tag{3.20}$$

$$= \frac{\sigma_d^2}{N} \sum_{i=-\infty}^{\infty} \mathbf{W}_i \cdot \mathbf{G}_1 \cdot \mathbf{G}_1^H \cdot \mathbf{W}_i^H \tag{3.21}$$

$$= \frac{\sigma_d^2}{N} \mathbf{I}_\infty \otimes \mathbf{G}_1 \mathbf{G}_1^H \tag{3.22}$$

where $\mathbf{G}_1 \mathbf{G}_1^H = \mathbf{G}_1 \mathbf{G}_1^T$ is a tri-diagonal matrix given by

$$\mathbf{G}_1 \mathbf{G}_1^T = \begin{bmatrix} \mathbf{I}_{N_{512}} & \mathbf{0} & \mathbf{I}_{N_{512}} \\ \mathbf{0} & \mathbf{I}_{N-N_{512}} & \mathbf{0} \\ \mathbf{I}_{N_{512}} & \mathbf{0} & \mathbf{I}_{N_{512}} \end{bmatrix}. \tag{3.23}$$

Because of the shape of the matrix $\mathbf{G}_1\mathbf{G}_1^T$, we consider partitioning the matrix $\mathbf{H}$ as

$$\mathbf{H} = [\cdots \quad \mathbf{H}_1 \quad \mathbf{H}_2 \quad \mathbf{H}_3 \quad \cdots] \tag{3.24}$$

$$= [\cdots \quad \mathbf{H}_{l1} \quad \mathbf{H}_{m1} \quad \mathbf{H}_{r1} \quad \mathbf{H}_{l2} \quad \mathbf{H}_{m2} \quad \mathbf{H}_{r2} \quad \cdots] \tag{3.25}$$

where $\mathbf{H}_i$ is the ith $N + N_{512}$ columns of $\mathbf{H}$, $\mathbf{H}_{li}$ and $\mathbf{H}_{ri}$ consist of the left most and right most N_{512} columns of $\mathbf{H}_i$, respectively, and $\mathbf{H}_{mi}$ is composed of the middle $N - N_{512}$ columns of $\mathbf{H}_i$. The autocorrelation matrix of received signals $\mathbf{r}$ is then given by

$$\mathbf{C}_r = E\left\{\mathbf{r}\cdot\mathbf{r}^H\right\} \tag{3.26}$$

$$= E\left\{(\mathbf{D}(\theta)\mathbf{A}(\epsilon)\mathbf{H}\mathbf{y} + \mathbf{w})(\mathbf{y}^H\mathbf{H}^H\mathbf{A}^H(\epsilon)\mathbf{D}^H(\theta) + \mathbf{w}^H)\right\} \tag{3.27}$$

$$= \frac{\sigma_d^2}{N}E\left\{\mathbf{D}(\theta)\mathbf{A}(\epsilon)\mathbf{H}\left(\mathbf{I}_\infty \otimes \mathbf{G}_1\mathbf{G}_1^H\right)\mathbf{H}^H\mathbf{A}^H(\epsilon)\mathbf{D}^H(\theta)\right\} + \sigma_w^2\mathbf{I} \tag{3.28}$$

$$= \frac{\sigma_d^2}{N}\mathbf{D}(\theta)\mathbf{A}(\epsilon)E\left(\mathbf{H}\mathbf{H}^H + \sum_{i=-\infty}^{\infty}\mathbf{H}_{ri}\mathbf{H}_{li}^H + \sum_{i=-\infty}^{\infty}\mathbf{H}_{li}\mathbf{H}_{ri}^H\right)\mathbf{A}^H(\epsilon)\mathbf{D}^H(\theta) + \sigma_w^2\mathbf{I}. \tag{3.29}$$

As mentioned, we assume that the length of the channel impulse response (CIR) is smaller than the CP length. Here we also assume the channel to be wide sense stationary uncorrelated scattering (WSSUS), that is,

$$E\{h(l,n)h^*(l+\Delta l, n+\Delta n)\} = \varphi_h(l,\Delta n)\delta(\Delta l) \tag{3.30}$$

where $\varphi_h(l,\Delta n)$, by the above assumption on CIR length, can be nonzero only when $0 \le l \le N_{512} - 1$.

The first term in the parenthesis of (3.29) leads to

$$E\left\{[\mathbf{H}\mathbf{H}^H]_{p,q}\right\} = \sum_{k=-\infty}^{\infty} E\left\{h(p-k,p)h^*(q-k,q)\right\} \tag{3.31}$$

$$= \sum_{l=\infty}^{-\infty} E\left\{h(l,p)h^*(l+(q-p),p+(q-p))\right\} \tag{3.32}$$

$$= \sum_{l=\infty}^{-\infty} \varphi_h(l,q-p)\delta(q-p) \tag{3.33}$$

$$= \sum_{l=0}^{N_{512}-1} \varphi_h(l,q-p)\delta(q-p). \tag{3.34}$$

Therefore, $E\{\sum_{i=-\infty}^{\infty}\mathbf{H}\mathbf{H}^H\}$ is a scaled identity matrix given by

$$E\left\{\mathbf{H}\mathbf{H}^H\right\} = \sum_{l=0}^{N_{512}-1}\varphi_h(l,0)\mathbf{I} \equiv \sigma_h^2\mathbf{I}. \tag{3.35}$$

The second term in the parenthesis of (3.29) leads to

$$E\left\{\left[\sum_{i=-\infty}^{\infty}\mathbf{H}_{ri}\mathbf{H}_{li}^H\right]_{p,q}\right\} = \sum_{i=-\infty}^{\infty}\sum_{k=0}^{N_{512}-1}E\left\{[\mathbf{H}_{ri}]_{p,k}[\mathbf{H}_{li}^H]_{q,k}\right\} \tag{3.36}$$

$$= \sum_{i=-\infty}^{\infty}\sum_{k=0}^{N_{512}-1}E\{h(p-iM_{512}-N-k,p)h^*(q-iM_{512}-k,q)\} \tag{3.37}$$

$$= \sum_{i=-\infty}^{\infty}\sum_{k=0}^{N_g-1}\varphi_h(p-iM_{512}-N-k,q-p)\delta(q-p+N) \tag{3.38}$$

where $M_{512} = N + N_{512}$. Similarly, the third term leads to

$$E\left\{\left[\sum_{i=-\infty}^{\infty}\mathbf{H}_{li}\mathbf{H}_{ri}^H\right]_{p,q}\right\} = \sum_{i=-\infty}^{\infty}\sum_{k=0}^{N_{512}-1}E\left\{[\mathbf{H}_{li}]_{p,k}[\mathbf{H}_{ri}^H]_{q,k}\right\} \tag{3.39}$$

$$= \sum_{i=-\infty}^{\infty}\sum_{k=0}^{N_{512}-1}E\{h(p-iM_{512}-k,p)h^*(q-iM_{512}-N-k,q)\} \tag{3.40}$$

$$= \sum_{i=-\infty}^{\infty}\sum_{k=0}^{N_g-1}\varphi_h(p-iM_{512}-k,q-p)\delta(q-p-N). \tag{3.41}$$

From (3.31) to (3.41), we see that $E\{\sum_{i=-\infty}^{\infty}\mathbf{H}_{ri}\mathbf{H}_{li}^H\}$ is a matrix with all its nonzero elements located on a certain subdiagonal, $E\{\sum_{i=-\infty}^{\infty}\mathbf{H}_{li}\mathbf{H}_{ri}^H\}$ is a matrix with all its nonzero elements located on a certain superdiagonal, and $E\{\mathbf{H}\mathbf{H}^H\}$ is a matrix with all its nonzero elements located on the diagonal. The matrix $\mathbf{C}_r$ is then given by

$$[\mathbf{C}_r]_{p,q} = \begin{cases} \frac{\sigma_d^2}{N}\sum_{k=0}^{N_{512}-1}\varphi_h(k,0)+\sigma_w^2 \equiv \sigma_r^2, & q=p, \\ \frac{\sigma_d^2}{N}e^{+j2\pi\epsilon}\sum_{i=-\infty}^{\infty}\sum_{k=0}^{N_{512}-1}\varphi_h(\theta_1+p-iM_{512}-N-k,-N), & q=p-N, \\ \frac{\sigma_d^2}{N}e^{-j2\pi\epsilon}\sum_{i=-\infty}^{\infty}\sum_{k=0}^{N_{512}-1}\varphi_h(\theta_1+p-iM_{512}-k,+N), & q=p+N, \\ 0, & \text{else.} \end{cases} \tag{3.42}$$

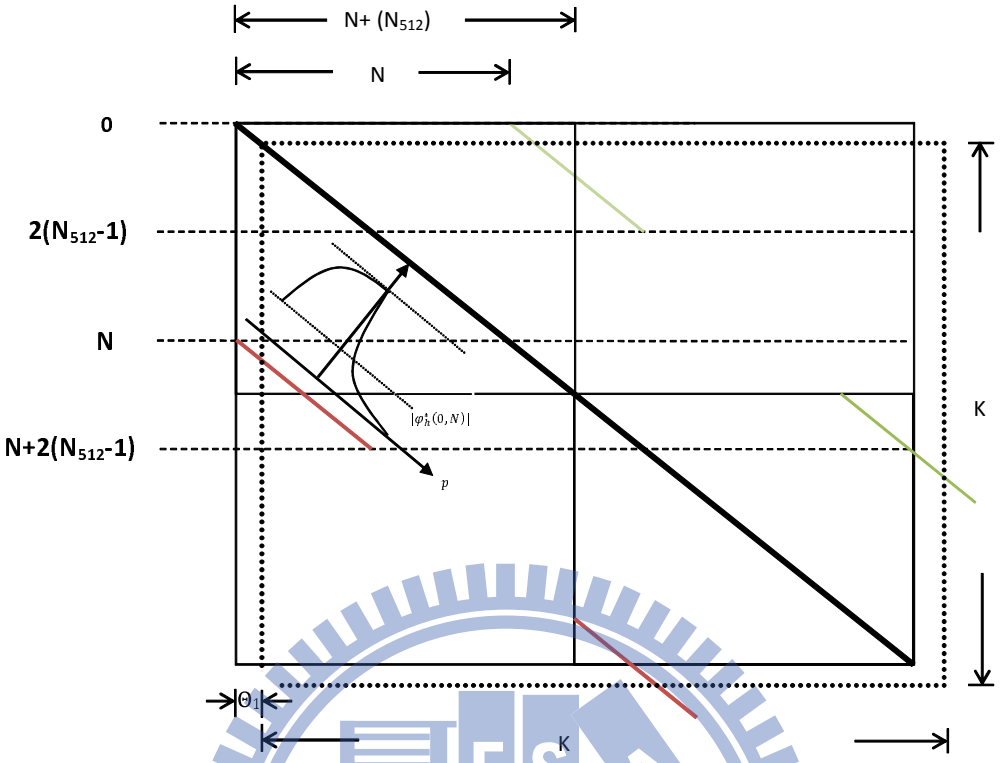

Figure 3.3: Structure of the autocorrelation matrix $\mathbf{C}_r$.

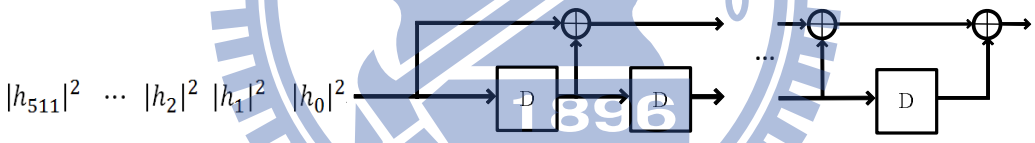

Figure 3.4: Moving average.

Figure 3.3 depicts the structure of autocorrelation matrix $\mathbf{C}_r$. First, the bold line on the diagonal indicates where the nonzero elements of $E\{\mathbf{H}\mathbf{H}^H\}$ are located and each of them has the same value σ_r^2. The two thinner lines along a subdiagonal and a superdiagonal, which appear like a long dashed line each, indicate where the nonzero elements of $E\{\sum_{i=-\infty}^{\infty}\mathbf{H}_{ri}\mathbf{H}_{li}^H\}$ and $E\{\sum_{i=-\infty}^{\infty}\mathbf{H}_{li}\mathbf{H}_{ri}^H\}$ may lie. These elements are not all of the same value along each diagonal, but each segment is given by a scaled version of the N_{512}-point moving average of the channel PDP. The xy-plot located near the first sequent of the subdiagonal in Figure 3.3 illustrates the concept, where for illustration purpose we assume that PDP has an exponential shape. Figure 3.4 illustrates the essence of the moving-average operation that results in the above property. Finally, the dotted square represents the matrix $\mathbf{C}_r \in C^{K\times K}$ when the

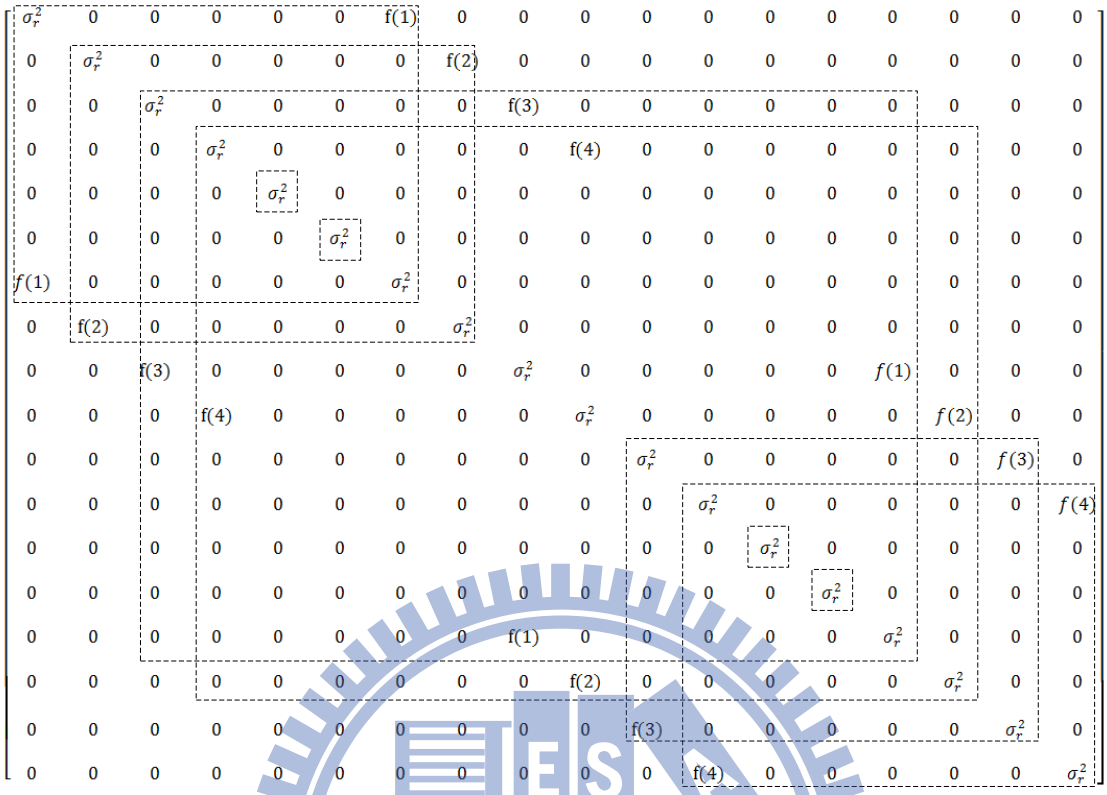

Figure 3.5: Autocorrelation matrix example.

observation window has a finite size K and located at an STO θ_1.

Note from (3.17) that we have to compute the inversion of $\mathbf{C}_r$. Due to its tridiagonal structure, a closed-form expression can be obtained that expresses the elements of $\mathbf{C}_r^{-1}$ in terms of that of $\mathbf{C}_r$. Before presenting the general form, we first give a simple example for illustration purpose. Consider a case with FFT size $N = 6$, CP length $N_g = 2$, observation window size $K = 18$, and STO $\theta_1 = 0$. The corresponding $\mathbf{C}_r$ is shown in Figure 3.5. From this figure, we can see that $\mathbf{C}_r$ can be divided into 3-by-3, 2-by-2 and 1-by-1 submatrix whose inverse can be computed separately to make up the full $\mathbf{C}_r^{-1}$. Thus the inversion of $\mathbf{C}_r$ can be obtained rather simply. For this example, the joint PDF of received signal $\mathbf{r}$ is given by

$$\begin{aligned} f(\mathbf{r}|\epsilon_1,\theta_1) \;=\; & \prod_{n\in\{0,1\}} \frac{f(r(n),r(n+N)|\epsilon_1,\theta_1)}{f(r(n)|\epsilon_1,\theta_1)\cdot f(r(n+N)|\epsilon_1,\theta_1)} \\ & \prod_{n\in\{2,3\}} \frac{f(r(n),r(n+N),r(n+2N)|\epsilon_1,\theta_1)}{f(r(n)|\epsilon_1,\theta_1)\cdot f(r(n+N)|\epsilon_1,\theta_1)\cdot f(r(n+2N)|\epsilon_1,\theta_1)} \\ & \prod_{n\in\{10,11\}} \frac{f(r(n),r(n+N)|\epsilon_1,\theta_1)}{f(r(n)|\epsilon_1,\theta_1)\cdot f(r(n+N)|\epsilon_1,\theta_1)} \prod_{n} f(r(n)|\epsilon_1,\theta_1) \end{aligned} \tag{3.43}$$

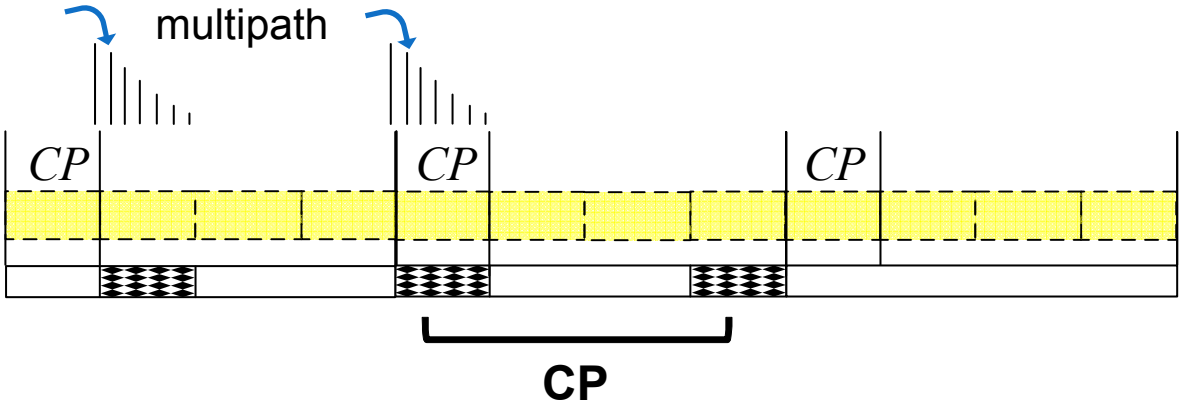

Figure 3.6: Three-region data correlation.

where

$$f(r(n), r(n+N)|\epsilon_1, \theta_1) = \frac{\exp\left(-\mathbf{r}_1^H \mathbf{C}_1^{-1} \mathbf{r}_1\right)}{\pi^2 \det(\mathbf{C}_1)}, \tag{3.44}$$

$$f(r(n), r(n+N), r(n+2N)|\epsilon_1, \theta_1) = \frac{\exp\left(-\mathbf{r}_2^H \mathbf{C}_2^{-1} \mathbf{r}_2\right)}{\pi^2 \det(\mathbf{C}_2)}, \tag{3.45}$$

$$f(r(n)|\epsilon_1, \theta_1) = \frac{\exp\left(-\frac{|r(n)|^2}{\sigma_r^2}\right)}{\pi\sigma_r^2}, \tag{3.46}$$

$$f(r(n+N)|\epsilon_1, \theta_1) = \frac{\exp\left(-\frac{|r(n+N)|^2}{\sigma_r^2}\right)}{\pi\sigma_r^2}, \tag{3.47}$$

$$f(r(n+2N)|\epsilon_1, \theta_1) = \frac{\exp\left(-\frac{|r(n+2N)|^2}{\sigma_r^2}\right)}{\pi\sigma_r^2}, \tag{3.48}$$

with $\mathbf{r}_1 = [r(n), r(n+N)]$, $\mathbf{r}_2 = [r(n), r(n+N), r(n+2N)]$, $\mathbf{C}_1$ and $\mathbf{C}_2$ are the autocorrelation matrixes of vectors $\mathbf{r}_1$ and $\mathbf{r}_2$, respectively.

From (3.43) we can see that there are three kinds of data correlation. The first is because of the CP structure. The second is due not only to the CP structure but also the multi-path channel spread, as illustrated in Figure 3.6. And the third is due to the multi-path channel spread alone.

Now consider a general FFT size N, CP length N_{512}, and STO θ_1. For illustration, consider an observation window size $K = 3M_{512}$. Figure 3.7 depicts the various conditions of data correlation. We divide an OFDM symbol into 4 sections, $R_I = \{m|N \leq m \leq M_{512}-1\}$, $R_{II} = \{m|0 \leq m \leq +N_{512}-1\}$, $R_{III} = \{m|N_{512} \leq m \leq 2N_{512}-1\}$, and $R_{IV} = \{m|2N_{512} \leq m \leq N-1\}$, where $m = [(n-\theta_1) \mod M_{512}]$ is the distance between timing index n and STO θ_1. In Figure 3.7, R_j^i denotes the ith region in section j under symbol timing offset

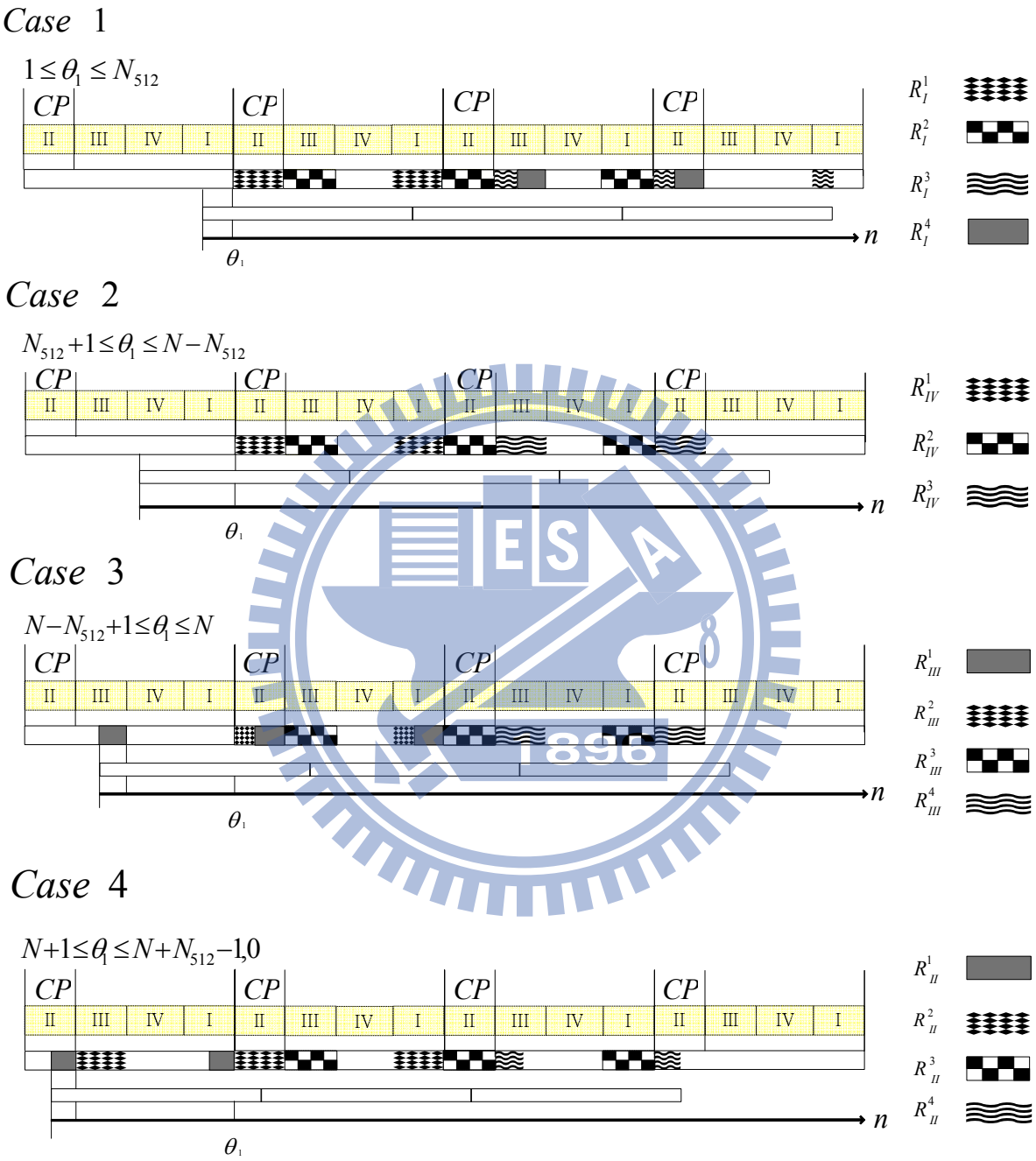

Figure 3.7: Relative positioning of observation window with respect to STO, as well as the correlation structure in the received signal.

θ_1, and there are four cases due to the different sections where in θ_1 is located. Noted that if the observation window is infinite, then data correlation is always over the three regions R_{III}, R_{II} and R_I. Two-region data correlation occurs only at the boundaries of the observation window which cuts one of three regions, R_{III} or R_I, out of the picture. The data that do not correlate with others are those that situate in the middle of an OFDM symbol and are not repeated in the CP or affected by the ring-down of the multipath spread caused to the signal in the CP.

From the previous discussion, we see that likelihood function is in general of the form

$$\begin{aligned} f(\mathbf{r}|\epsilon_1,\theta_1) &= \prod_{n\in R_0} \frac{f(r(n),r(n+N)|\epsilon_1,\theta_1)}{f(r(n)|\epsilon_1,\theta_1)\cdot f(r(n+N)|\epsilon_1,\theta_1)} \\ &\quad \prod_{n\in R_1} \frac{f(r(n),r(n+N),r(n+2N)|\epsilon,\theta_1)}{f(r(n)|\epsilon_1,\theta_1)\cdot f(r(n+N)|\epsilon_1,\theta_1)\cdot f(r(n+2N)|\epsilon_1,\theta_1)} \\ &\quad \prod_{n\in R_2} \frac{f(r(n),r(n+N)|\epsilon_1,\theta_1)}{f(r(n)|\epsilon_1,\theta_1)\cdot f(r(n+N)|\epsilon_1,\theta_1)} \prod_n f(r(n)|\epsilon_1,\theta_1), \end{aligned} \tag{3.49}$$

where

$$\begin{aligned} R_0 &= \{m|0\le m\le N_{512}-1\}\cap\{n<N\}\cap\{n+N\le K\}, \\ R_1 &= \{m|N_{512}\le m\le 2N_{512}-1\}\cap\{n+2N\le K\}, \\ R_2 &= \{m|N_{512}\le m\le 2N_{512}-1\}\cap\{n+2N>K\}\cap\{n+N\le K\}, \end{aligned} \tag{3.50}$$

with $m=(n-\theta_1) \mod M_{512}$.

According to (3.49) and (3.50), the log-likelihood function of the received signals $\mathbf{r}$ can be written as

$$\begin{aligned} \Lambda_1(\theta_1,\epsilon_1) &= \log\left[\prod_{n\in R_0} \frac{f(r(n),r(n+N)|\epsilon_1,\theta_1)}{f(r(n)|\epsilon_1,\theta_1)\cdot f(r(n+N)|\epsilon_1,\theta_1)}\right] \\ &\quad +\log\left[\prod_{n\in R_1} \frac{f(r(n),r(n+N),r(n+2N)|\epsilon_1,\theta_1)}{f(r(n)|\epsilon_1,\theta_1)\cdot f(r(n+N)|\epsilon_1,\theta_1)\cdot f(r(n+2N)|\epsilon_1,\theta_1)}\right] \\ &\quad +\log\left[\prod_{n\in R_2} \frac{f(r(n),r(n+N)|\epsilon_1,\theta_1)}{f(r(n)|\epsilon_1,\theta_1)\cdot f(r(n+N)|\epsilon_1,\theta_1)}\right] + \log\left[\prod_n f(r(n)|\epsilon_1,\theta_1)\right] \end{aligned} \tag{3.51}$$

$$= \sum_{n\in R_0\bigcup R_2} \Phi_1(n,\epsilon_1,\theta_1) + \sum_{n\in R_1} \Phi_2(n,\epsilon_1,\theta_1) + \log\left[\prod_n f(r(n)|\epsilon_1,\theta_1)\right] \tag{3.52}$$

where

$$\Phi_1(n,\epsilon_1,\theta_1) \equiv \log \frac{f(r(n),r(n+N)|\epsilon_1,\theta_1)}{f(r(n)|\epsilon_1,\theta_1)\cdot f(r(n+N)|\epsilon_1,\theta_1)} \tag{3.53}$$

$$= \frac{-|\rho(m)|^2\left(|r(n)|^2+|r(n+N)|^2\right)}{\sigma_r^2(1-|\rho(m)|^2)} + 2\Re\left\{\frac{r(n)r^*(n+N)\rho(m)}{\sigma_r^2(1-|\rho(m)|^2)}e^{+j2\pi\epsilon_1}\right\}$$

$$-\log(1-|\rho(m)|^2) \tag{3.54}$$

and

$$\Phi_2(n,\epsilon_1,\theta_1) \equiv \log \frac{f(r(n),r(n+N),r(n+2N)|\epsilon_1,\theta_1)}{f(r(n)|\epsilon_1,\theta_1)\cdot f(r(n+N)|\epsilon_1,\theta_1)\cdot f(r(n+2N)|\epsilon_1,\theta_1)} \tag{3.55}$$

$$= \frac{-|\rho(m)|^2\left(|r(n)|^2+|r(n+N)|^2\right)-|\rho(m-N_{512})|^2\left(|r(n+N)|^2+|r(n+2N)|^2\right)}{\sigma_r^2(1-|\rho(m)|^2-|\rho(m-N_{512})|^2)}$$

$$+2\Re\left\{\frac{r(n)r^*(n+N)\rho(m)+r(n+N)r^*(n+2N)\rho(m-N_{512})}{\sigma_r^2(1-|\rho(m)|^2-|\rho(m-N_{512})|^2)}e^{+j2\pi\epsilon_1}\right\}$$

$$-2\Re\left\{\frac{r(n)r^*(n+2N)\rho(m)\rho(m-N_{512})}{\sigma_r^2(1-|\rho(m)|^2-|\rho(m-N_{512})|^2)}e^{+j4\pi\epsilon_1}\right\}$$

$$-\log(1-|\rho(m)|^2-|\rho(m-N_{512})|^2) \tag{3.56}$$

with $\rho(m)=\frac{\beta}{\sigma_r^2}\cdot\sum_{k=0}^{N_{512}-1}\varphi_h(m-k,N)$ and $\beta=\frac{\sigma_d^2}{N}$.

Assume that the Doppler spectrum follows the classical Jakes model. Then

$$\rho(m)=\frac{10^{SNR/10}J_0(2\pi f_dT)\cdot\sum_{k=0}^{N_{512}-1}\varphi_h(m-k,0)}{10^{SNR/10}J_0(2\pi f_dT)\cdot\sigma_h^2+1} \tag{3.57}$$

where $SNR\equiv\sigma_d^2/N$, $J_0(\cdot)$ is the zero-order Bessel function of first kind, f_d is the maximum Doppler shift and T is the useful symbol period.

First, from (3.46), we can see the product $\prod_n f(r(n)|\epsilon_1,\theta_1)$ is independent of θ_1 and ϵ_1; so we can drop this term. Second, according to (3.54) and (3.56), we can group these terms into two types, one including the effect of the CFO ϵ_1, the other not. Thus the log-likelihood

function can be rewritten as

$$\Lambda_1(\theta_1,\epsilon_1) = \left(\sum_{n\in R_0\bigcup R_2}\lambda_1(n,\theta_1)+\sum_{n\in R_1}\lambda_2(n,\theta_1)\right)+2\Re\left\{\left(\sum_{n\in R_0\bigcup R_2}T_1(n,\theta_1)\right)e^{+j2\pi\epsilon_1}\right\}$$
$$+2\Re\left\{\left(\sum_{n\in R_1}T_2(n,\theta_1)\right)e^{+j2\pi\epsilon_1}\right\}-2\Re\left\{\left(\sum_{n\in R_1}T_3(n,\theta_1)\right)e^{+j4\pi\epsilon_1}\right\} \quad (3.58)$$

$$= A_1(n,\theta_1)+2\left|A_2(n,\theta_1)\right|\cos\left(2\pi\epsilon_1+\angle A_2(n,\theta_1)\right)$$

$$-2\left|A_3(n,\theta_1)\right|\cos\left(4\pi\epsilon_1+\angle A_3(n,\theta_1)\right), \quad (3.59)$$

where

$$A_1(n,\theta_1) = \sum_{n\in R_0\bigcup R_2}\lambda_1(n,\theta_1)+\sum_{n\in R_1}\lambda_2(n,\theta_1), \quad (3.60)$$

$$A_2(n,\theta_1) = \sum_{n\in R_0\bigcup R_2}T_1(n,\theta_1)+\sum_{n\in R_1}T_2(n,\theta_1), \quad (3.61)$$

$$A_3(n,\theta_1) = \sum_{n\in R_1}T_3(n,\theta_1), \quad (3.62)$$

with

$$\lambda_1(n,\theta_1) = \frac{-|\rho(m)|^2\left(|r(n)|^2+|r(n+N)|^2\right)}{\sigma_r^2(1-|\rho(m)|^2)}-\log(1-|\rho(m)|^2), \quad (3.63)$$

$$\lambda_2(n,\theta_1) = \frac{-|\rho(m)|^2\left(|r(n)|^2+|r(n+N)|^2\right)-|\rho(m-N_{512})|^2\left(|r(n+N)|^2+|r(n+2N)|^2\right)}{\sigma_r^2(1-|\rho(m)|^2-|\rho(m-N_{512})|^2)}$$

$$-\log(1-|\rho(m)|^2-|\rho(m-N_{512})|^2), \quad (3.64)$$

and

$$T_1(n,\theta_1) = \frac{r(n)r^*(n+N)\rho(m)}{\sigma_r^2(1-|\rho(m)|^2)}, \quad (3.65)$$

$$T_2(n,\theta_1) = \frac{r(n)r^*(n+N)\rho(m)+r(n+N)r^*(n+2N)\rho(m-N_{512})}{\sigma_r^2(1-|\rho(m)|^2-|\rho(m-N_{512})|^2)}, \quad (3.66)$$

$$T_3(n,\theta_1) = \frac{r(n)r^*(n+2N)\rho(m)\rho(m-N_{512})}{\sigma_r^2(1-|\rho(m)|^2-|\rho(m-N_{512})|^2)}. \quad (3.67)$$

3.2.2 Derivation of the likelihood function for normal CP

The derivation of algorithm for normal CP is similar to that for extended CP except that we have to modify the region size and location and change some parameters.

For normal CP, we set the observation window size K is large enough to comprise the slot timing θ_2, and we then modify the likelihood function in (3.49) as

$$\begin{aligned} f(\mathbf{r}|\epsilon_2,\theta_2) &= \prod_{n\in R_0}\frac{f(r(n),r(n+N)|\epsilon_2,\theta_2)}{f(r(n)|\epsilon_2,\theta_2)\cdot f(r(n+N)|\epsilon_2,\theta_1)} \\ &\quad \prod_{n\in R_1}\frac{f(r(n),r(n+N),r(n+2N)|\epsilon,\theta_2)}{f(r(n)|\epsilon_2,\theta_2)\cdot f(r(n+N)|\epsilon_2,\theta_2)\cdot f(r(n+2N)|\epsilon_2,\theta_2)} \\ &\quad \prod_{n\in R_2}\frac{f(r(n),r(n+N)|\epsilon_2,\theta_2)}{f(r(n)|\epsilon_2,\theta_2)\cdot f(r(n+N)|\epsilon_2,\theta_2)}\prod_{n\in R_3}\frac{f(r(n),r(n+N)|\epsilon_2,\theta_2)}{f(r(n)|\epsilon_2,\theta_2)\cdot f(r(n+N)|\epsilon_2,\theta_2)} \\ &\quad \prod_{n} f(r(n)|\epsilon_2,\theta_2), \end{aligned} \tag{3.68}$$

where

$$\begin{aligned} R_0 &= \{m|0\le m\le N_{144}-1\}\cap\{n<N\}\cap\{n+N\le K\}, \\ R_1 &= \{m|N_{144}\le m\le 2N_{144}-1\}\cap\{n+2N\le K\}, \\ R_2 &= \{m|N_{144}\le m\le 2N_{144}-1\}\cap\{n+2N>K\}\cap\{n+N\le K\}, \\ R_3 &= \{n|\theta_2+N_{144}\le n\le \theta_2+N_{160}-1\}\cap\{n+N\le K\}, \end{aligned} \tag{3.69}$$

with

$$m=\begin{cases} (n-\theta_2) \mod M_{144}, & n<(\theta_2+N_{144}), \\ N_{144}-1, & (\theta_2+N_{144})\le n\le(\theta_2+N_{160}-1), \\ (n-(N_{160}-N_{144})-\theta_2) \mod M_{144}, & \text{else.} \end{cases} \tag{3.70}$$

From the previous discussion, we can conclude that the log-likelihood function can be written as

$$\begin{aligned} \Lambda_2(\theta_2,\epsilon_2) &= \left(\sum_{n\in R_0\bigcup R_2\bigcup R_3}\gamma_1(n,\theta_2)+\sum_{n\in R_1}\gamma_2(n,\theta_2)\right)+2\Re\left\{\left(\sum_{n\in R_0\bigcup R_2\bigcup R_3}D_1(n,\theta_2)\right)e^{+j2\pi\epsilon_2}\right\} \\ &\quad +2\Re\left\{\left(\sum_{n\in R_1}D_2(n,\theta_2)\right)e^{+j2\pi\epsilon_2}\right\}-2\Re\left\{\left(\sum_{n\in R_1}D_3(n,\theta_2)\right)e^{+j4\pi\epsilon_2}\right\} \end{aligned} \tag{3.71}$$

$$\begin{aligned} &= B_1(n,\theta_2)+2\left|B_2(n,\theta_2)\right|\cos\left(2\pi\epsilon_2+\angle B_2(n,\theta_2)\right) \\ &\quad -2\left|B_3(n,\theta_2)\right|\cos\left(4\pi\epsilon_2+\angle B_3(n,\theta_2)\right), \end{aligned} \tag{3.72}$$

where

$$B_1(n,\theta_2) = \sum_{n\in R_0\bigcup R_2\bigcup R_3}\gamma_1(n,\theta_2)+\sum_{n\in R_1}\gamma_2(n,\theta_2), \tag{3.73}$$

$$B_2(n,\theta_2) = \sum_{n\in R_0\bigcup R_2\bigcup R_3}D_1(n,\theta_2)+\sum_{n\in R_1}D_2(n,\theta_2), \tag{3.74}$$

$$B_3(n,\theta_2) = \sum_{n\in R_1}D_3(n,\theta_2), \tag{3.75}$$

with

$$\gamma_1(n,\theta_2) = \frac{-|\omega(m)|^2\left(|r(n)|^2+|r(n+N)|^2\right)}{\sigma_r^2(1-|\omega(m)|^2)}-\log(1-|\omega(m)|^2), \tag{3.76}$$

$$\gamma_2(n,\theta_2) = \frac{-|\omega(m)|^2\left(|r(n)|^2+|r(n+N)|^2\right)-|\omega(m-N_{144})|^2\left(|r(n+N)|^2+|r(n+2N)|^2\right)}{\sigma_r^2(1-|\omega(m)|^2-|\omega(m-N_{144})|^2)}$$

$$-\log(1-|\omega(m)|^2-|\omega(m-N_{144})|^2), \tag{3.77}$$

and

$$D_1(n,\theta_2) = \frac{r(n)r^*(n+N)\omega(m)}{\sigma_r^2(1-|\omega(m)|^2)}, \tag{3.78}$$

$$D_2(n,\theta_2) = \frac{r(n)r^*(n+N)\omega(m)+r(n+N)r^*(n+2N)\omega(m-N_{144})}{\sigma_r^2(1-|\omega(m)|^2-|\omega(m-N_{144})|^2)}, \tag{3.79}$$

$$D_3(n,\theta_2) = \frac{r(n)r^*(n+2N)\omega(m)\omega(m-N_{144})}{\sigma_r^2(1-|\omega(m)|^2-|\omega(m-N_{144})|^2)}, \tag{3.80}$$

with

$$\omega(m)=\frac{10^{SNR/10}J_0(2\pi f_dT)\cdot\sum_{k=0}^{N_{144}-1}\varphi_h(m-k,0)}{10^{SNR/10}J_0(2\pi f_dT)\cdot\sigma_h^2+1}. \tag{3.81}$$

3.2.3 Joint estimation of STO, CFO, and CP type

From (3.59), the joint estimation for θ_1 and ϵ_1 can be achieved as follows:

$$\max_{\theta_1,\epsilon_1}\Lambda_1(\theta_1,\epsilon_1)=\max_{\theta_1\in\{0,1,\cdots,K-1\}}\max_{\epsilon_1|\theta_1}\Lambda_1(\theta_1,\epsilon_1), \tag{3.82}$$

that is, θ_1 takes a value from 0 to $K-1$ (the observation window size), and for each θ_1, the corresponding ϵ_1 is computed, which entails a solution of a 4th-order polynomial equation. Because by doing so, the complexity will be very high, we consider an approximation. We

assume that if the set $\{n|n \in R_1\}$ is large enough, then the angle of $A_3(n,\theta_1)$ is close to $-4\pi\epsilon_1$, and so the last cosine term in (3.59) is close to one. Thus, the log-likelihood function becomes

$$\Lambda_1(\theta_1,\epsilon_1) \approx A_1(n,\theta_1) + 2\left|A_2(n,\theta_1)\right|\cos\left(2\pi\epsilon_1 + \angle\left(A_2(n,\theta_1)\right)\right) - 2\left|A_3(n,\theta_1)\right|. \tag{3.83}$$

Maximizing the approximate log-likelihood function (3.83), we get the joint quasi-ML estimation of θ_1 and ϵ_1 in two steps as

$$\arg\max_{\theta_1,\epsilon_1} \Lambda_1(\theta_1,\epsilon_1) = \arg\max_{\theta_1}\max_{\epsilon_1|\theta_1} \Lambda_1(\theta_1,\epsilon_1) = \arg\max_{\theta_1} \Lambda_1(\theta_1,\hat{\epsilon}_1(\theta_1)). \tag{3.84}$$

For each θ_1, the maximization of $\Lambda_1(\theta_1,\epsilon_1)$ with respect to ϵ_1 is achieved with the cosine term in (3.83) equal to one. This yields

$$\hat{\epsilon}_1(\theta_1) = -\frac{1}{2\pi}\angle A_2(n,\theta_1) + n \tag{3.85}$$

where n is an integer. In this work, we assume $|\epsilon_1| < 0.5$; thus $n = 0$. With the cosine term in (3.83) equal to one, the log-likelihood function becomes

$$\Lambda_1(\theta_1,\hat{\epsilon}_1(\theta_1)) = A_1(n,\theta_1) + 2\left|A_2(n,\theta_1)\right| - 2\left|A_3(n,\theta_1)\right|. \tag{3.86}$$

Finally, the estimation of θ_1 for extended CP can be obtained as

$$\hat{\theta}_1 = \arg\max_{\theta_1}\left\{A_1(n,\theta_1) + 2\left(\left|A_2(n,\theta_1)\right| - \left|A_3(n,\theta_1)\right|\right)\right\}. \tag{3.87}$$

Similarly, the joint estimation of θ_2 and ϵ_2 for normal CP is given by

$$\hat{\theta}_2 = \arg\max_{\theta_2}\left\{B_1(n,\theta_2) + 2\left(\left|B_2(n,\theta_2)\right| - \left|B_3(n,\theta_2)\right|\right)\right\}, \tag{3.88}$$

$$\hat{\epsilon}_2(\theta_2) = -\frac{1}{2\pi}\angle B_2(n,\hat{\theta}_2). \tag{3.89}$$

In summary, the overall joint estimation of STO, CFO, and CP type is given by

$$\{\hat{\theta},\hat{\epsilon},\hat{m}\} = \max_{\theta,\epsilon,m} f(\mathbf{r}|\theta,\epsilon,m) = \max_{m}\max_{\theta|m}\max_{\epsilon|\theta,m} \Lambda(\mathbf{r}|\theta,\epsilon). \tag{3.90}$$

Tables 3.1 and 3.2 give a summary of the solution and various quantities defined in the derivation of the solution.

Table 3.1: Joint Estimation of STO, CFO for Extended CP

Estimator	$\hat{\theta}_1 = \arg\max_{\theta_1} \{A_1(n,\theta_1) + 2(\lvert A_2(n,\theta_1)\rvert - \lvert A_3(n,\theta_1)\rvert)\}$ $\hat{\epsilon}_1(\theta_1) = -\frac{1}{2\pi}\angle A_2(n,\hat{\theta}_1)$
Regions	$R_0 = \{m \lvert 0 \le m \le N_{512}-1\} \cap \{n < N\} \cap \{n+N \le K\}$ $R_1 = \{m \lvert N_{512} \le m \le 2N_{512}-1\} \cap \{n+2N \le K\}$ $R_2 = \{m \lvert N_{512} \le m \le 2N_{512}-1\} \cap \{n+2N > K\} \cap \{n+N \le K\}$ $m = (n-\theta_1) \mod M_{512}$
$A_1(n,\theta_1)$	$\sum_{n \in R_0 \bigcup R_2} \lambda_1(n,\theta_1) + \sum_{n \in R_1} \lambda_2(n,\theta_1)$
$A_2(n,\theta_1)$	$\sum_{n \in R_0 \bigcup R_2} T_1(n,\theta_1) + \sum_{n \in R_1} T_2(n,\theta_1)$
$A_3(n,\theta_1)$	$\sum_{n \in R_1} T_3(n,\theta_1)$
$\lambda_1(n,\theta_1)$	$-\frac{\lvert\rho(m)\rvert^2\left(\lvert r(n)\rvert^2 + \lvert r(n+N)\rvert^2\right)}{\sigma_r^2(1-\lvert\rho(m)\rvert^2)} - \log(1-\lvert\rho(m)\rvert^2)$
$\lambda_2(n,\theta_1)$	$-\frac{\lvert\rho(m)\rvert^2\left(\lvert r(n)\rvert^2 + \lvert r(n+N)\rvert^2\right) + \lvert\rho(m-N_{512})\rvert^2\left(\lvert r(n+N)\rvert^2 + \lvert r(n+2N)\rvert^2\right)}{\sigma_r^2(1-\lvert\rho(m)\rvert^2 - \lvert\rho(m-N_{512})\rvert^2)}$ $-\log(1-\lvert\rho(m)\rvert^2 - \lvert\rho(m-N_{512})\rvert^2)$
$T_1(n,\theta_1)$	$\frac{r(n)r^*(n+N)\rho(m)}{\sigma_r^2(1-\lvert\rho(m)\rvert^2)}$
$T_2(n,\theta_1)$	$\frac{r(n)r^*(n+N)\rho(m) + r(n+N)r^*(n+2N)\rho(m-N_{512})}{\sigma_r^2(1-\lvert\rho(m)\rvert^2 - \lvert\rho(m-N_{512})\rvert^2)}$
$T_3(n,\theta_1)$	$\frac{r(n)r^*(n+2N)\rho(m)\rho(m-N_{512})}{\sigma_r^2(1-\lvert\rho(m)\rvert^2 - \lvert\rho(m-N_{512})\rvert^2)}$
$\rho(m)$	$\frac{10^{SNR/10}J_0(2\pi f_d T)\cdot\sum_{k=0}^{N_{512}-1}\varphi_h(m-k,N)}{10^{SNR/10}J_0(2\pi f_d T)\cdot\sigma_h^2+1}$

Table 3.2: Joint Estimation of STO, CFO for Normal CP

Estimator	$\hat{\theta}_2 = \arg\max_{\theta_2} \{B_1(n,\theta_2) + 2\left(\lvert B_2(n,\theta_2)\rvert - \lvert B_3(n,\theta_2)\rvert\right)\}$ $\hat{\epsilon}_2(\theta_2) = -\frac{1}{2\pi}\angle B_2(n,\hat{\theta}_2)$
Regions	$R_0 = \{m\lvert 0 \le m \le N_{144}-1\} \cap \{n < N\} \cap \{n+N \le K\}$ $R_1 = \{m\lvert N_{144} \le m \le 2N_{144}-1\} \cap \{n+2N \le K\}$ $R_2 = \{m\lvert N_{144} \le m \le 2N_{144}-1\} \cap \{n+2N > K\} \cap \{n+N \le K\}$ $R_3 = \{n\lvert \theta_2+N_{144} \le n \le \theta_2+N_{160}-1\} \cap \{n+N \le K\}$ $m = \begin{cases} (n-\theta_2) \mod M_{144}, & n < (\theta_2+N_{144}) \\ N_{144}-1, & (\theta_2+N_{144}) \le n \le (\theta_2+N_{160}-1) \\ (n-(N_{160}-N_{144})-\theta_2) \mod M_{144}, & \text{else} \end{cases}$
$B_1(n,\theta_2)$	$\sum_{n\in R_0 \bigcup R_2 \bigcup R_3} \gamma_1(n,\theta_2) + \sum_{n\in R_1} \gamma_2(n,\theta_2)$
$B_2(n,\theta_2)$	$\sum_{n\in R_0 \bigcup R_2 \bigcup R_3} D_1(n,\theta_2) + \sum_{n\in R_1} D_2(n,\theta_2)$
$B_3(n,\theta_1)$	$\sum_{n\in R_1} D_3(n,\theta_2)$
$\gamma_1(n,\theta_2)$	$-\frac{\lvert\omega(m)\rvert^2\left(\lvert r(n)\rvert^2+\lvert r(n+N)\rvert^2\right)}{\sigma_r^2(1-\lvert\omega(m)\rvert^2)} - \log(1-\lvert\omega(m)\rvert^2)$
$\gamma_2(n,\theta_2)$	$-\frac{\lvert\omega(m)\rvert^2\left(\lvert r(n)\rvert^2+\lvert r(n+N)\rvert^2\right)+\lvert\omega(m-N_{144})\rvert^2\left(\lvert r(n+N)\rvert^2+\lvert r(n+2N)\rvert^2\right)}{\sigma_r^2(1-\lvert\omega(m)\rvert^2-\lvert\omega(m-N_{144})\rvert^2)}$ $-\log(1-\lvert\omega(m)\rvert^2-\lvert\omega(m-N_{144})\rvert^2)$
$D_1(n,\theta_2)$	$\frac{r(n)r^*(n+N)\omega(m)}{\sigma_r^2(1-\lvert\omega(m)\rvert^2)}$
$D_2(n,\theta_2)$	$\frac{r(n)r^*(n+N)\omega(m)+r(n+N)r^*(n+2N)\omega(m-N_{144})}{\sigma_r^2(1-\lvert\omega(m)\rvert^2-\lvert\omega(m-N_{144})\rvert^2)}$
$D_3(n,\theta_2)$	$\frac{r(n)r^*(n+2N)\omega(m)\omega(m-N_{144})}{\sigma_r^2(1-\lvert\omega(m)\rvert^2-\lvert\omega(m-N_{144})\rvert^2)}$
$\omega(m)$	$\frac{10^{SNR/10}J_0(2\pi f_d T)\cdot\sum_{k=0}^{N_{144}-1}\varphi_h(m-k,N)}{10^{SNR/10}J_0(2\pi f_d T)\cdot\sigma_h^2+1}$

Chapter 4

Simulation Results and Analysis

In this chapter we first give the simulation conditions. Then we present and analyze some simulation results for LTE-A systems with our quasi-ML synchronization method derived previously. Our focus is on the performance in detecting the CP type.

4.1 Simulation Conditions

We consider the FDD mode of LTE-A system in the SISO operating condition. The system parameters used are listed in Table 4.1.

We consider the following channel models: AWGN, single-path Rayleigh, Standford University Interim (SUI) and Pedestrian B (PB), which is one of the ITU-R models. The SUI channel models consist of 6 different radio channel models in three terrain categories [3]. The three terrain types corresponding to the SUI channels in suburban area are shown in Table 4.2.

SUI-1 and SUI-2 are Rician multi-path channels, whereas the other four are Rayleigh multi-path channels which exhibit greater root-mean-square (RMS) delay spread. The SUI-2 represents a worst-case condition for terrain type C. For the SUI channels, we only consider the modified SUI-1 to SUI-4 models in our simulation such that the CIR lengths are less than the minimum CP length.

The channel characteristics of SUI-1 to SUI-4 and Pedestrian B are shown in Tables 4.3–4.7. Since the power delay profiles (PDPs) of those channel models are based on actual measurements, it may not be equal to integer multiples of the sampling period in the LTE-A system. In computing, it will cost a very large amount of memory if we directly call

Table 4.1: Downlink System Parameters Used in Simulation

Parameters	Setting
Carrier frequency	2.5 GHz
Bandwidth	1.4 MHz
Sampling frequency	1.92 MHz
FFT size	128
CP types	Extended, Normal
CP lengths ($N_{512},\ N_{160},\ N_{144}$)	32, 10, 9
Modulation type	16 QAM
Channel models	Modified SUI-1, SUI-2, SUI-3, SUI-4
Normalized CFO	$[-0.5, 0.5]$
STO	$[1, M]$
Velocity	3 km, 120 km, 360 km
Window size	$2N\ +\ 1N_{512}$ $6N\ +\ 5N_{512}$

Table 4.2: SUI Channel Models for Three Terrain Types

Terrain type	Description	SUI channels
A	Hilly terrain, heavy tree	SUI-5, SUI-6
B	Between A and C	SUI-3, SUI-4
C	Flat terrain, light tree	SUI-1, SUI-2

Table 4.3: SUI-1 Channel Model

	Relative delay (μs or sample number)		Average power	
Tap	μs	sample numbers	dB	normalized dB
1	0	0	0	-0.1771
2	0.4	1	-15	-15.1771
3	0.9	2	-20	-20.1771

"$filter()$" function in MATLAB. So we modify the PDPs to solve the problem. The term $modified$ means that PDP is adjusted by forcing the CIR taps into integer multiples of the sampling period by rounding delays. This method is to shift the taps into the closest sampling instances, for preserving the path number and the path powers. Figure 4.1 depicts the method of rounding. Because the system bandwidth we used for simulation is 1.4 MHz, some of taps of PB channel in this case will overlap on the same sample, and for them we adjust the PDP path locations in order to avoid overlapping.

Table 4.4: SUI-2 Channel Model

	Relative delay (μs or sample number)		Average power	
Tap	μs	sample numbers	dB	normalized dB
1	0	0	0	−0.3930
2	0.4	1	−12	−12.3930
3	1.1	2	−15	−15.3930

Table 4.5: SUI-3 Channel Model

	Relative delay (μs or sample number)		Average power	
Tap	μs	sample numbers	dB	normalized dB
1	0	0	0	−1.5113
2	0.4	1	−5	−6.5113
3	0.9	2	−10	−11.5113

Table 4.6: SUI-4 Channel Model

	Relative delay (μs or sample number)		Average power	
Tap	μs	sample numbers	dB	normalized dB
1	0	0	0	−1.9218
2	1.5	3	−4	−5.9218
3	4	8	−8	−9.9218

Table 4.7: PB Channel Model

	Relative delay (μs or sample number)		Average power	
Tap	μs	sample numbers	dB	normalized dB
1	0	0	0	−3.9114
2	0.2→0.3	0→1	−0.9	−4.8114
3	0.8	2	−4.9	−8.8114
4	1.2→1.5	2→3	−8	−11.9114
5	2.3	4	−7.9	−11.8114
6	3.7	7	−23.9	−27.8114

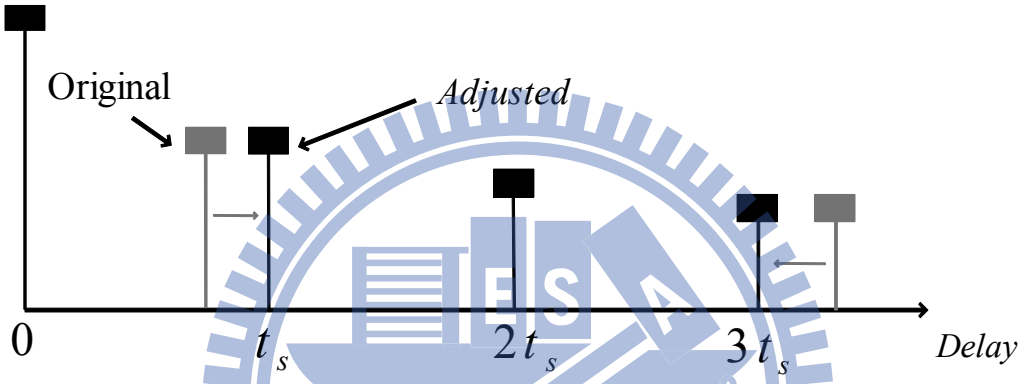

Figure 4.1: Tap location adjustment by rounding to integer sample spacing.

4.2 Simulation Method

We describe the simulation setting and computational flow in this section.

The simulation result under this environment is based on observing the error rate of the CP type. First, we construct a two-slot long transmitted signal in the time domain with a random CP type. Then we put the transmitting signals into channel by calling "$filter()$" function after setting up channel parameters by calling the "*awgn*" or "*rayleighchan*" function in MATLAB. Finally, we estimate the error rate of CP type at the receiver side. In the following sections, all the results shown in the figures are averages over 2×10^5 runs.

The estimation process can be devided into several steps as follows:

- Step 1: Use (3.87) and (3.88) to find the STOs θ_1 and θ_2.
- Step 2: Substitute the estimated θ_1 and θ_2 into (3.85) and (3.89) to find the CFOs ϵ_1 and ϵ_2.

- Step 3: Compare the log-likelihood function values corresponding to the two different CP types and pick the one having the larger value.

4.3 CP Type Estimation Performance with A Small Observation Window

We consider the CP type estimation performance at an observation window size of $2N_{fft}+N_{512}$ in this section. The channels simulated include AWGN, single-path Rayleigh, and multipath fading channels.

4.3.1 AWGN and Single-Path Rayleigh Fading Channels

Figures 4.2 and 4.3 show the performance of the CP detection error rate in AWGN and single-path Rayleigh channels, respectively. In these figures, the lines with "CP1" legend mean the error rate of that eNB transmits the extended CP type (denoted CP1 for simplify), but the receiver detects to the normal CP type (denoted CP2 for simplify). And the lines with "CP2" legend mean the error rate of that eNB transmits the CP2 type, but the receiver detects to the CP1 type.

From these figures, the performance for transmitting CP1 type is much better (having less error) than the other. This can be explained as follows. Because the channel considered in these two cases are AWGN and single-path Rayleigh, the data that are correlated are just in two regions due to the CP structure (with no effect of spread of multi-path channel). And we assume that the log-likelihood function is maximized when the observed window includes the maximum pairs of correlated data.

Figure 4.4 depicts the window sliding structure that captures the essence. If CP1 type is transmitted, the numbers of maximum pairs of correlated data are always N_{512} for the CP1 estimator, and they are changed with maximum value $N_{160}+N_{144}$ for the CP2 estimator. The difference of maximum number of pairs between CP1 estimator and CP2 estimator with transmitting CP1 type is $N_{512}-(N_{160}+N_{144})$.

However, if CP2 type is transmitted, the maximum number of pairs of correlated data is $N_{160}+N_{144}$ for the CP2 estimator, while it is $N_{160}+N_{144}$ (the same value) for the CP1 estimator. There is no difference of maximum number of pairs between CP1 estimator and CP2 estimator with transmitting CP2 type. Figure 4.5 shows the maximum number of

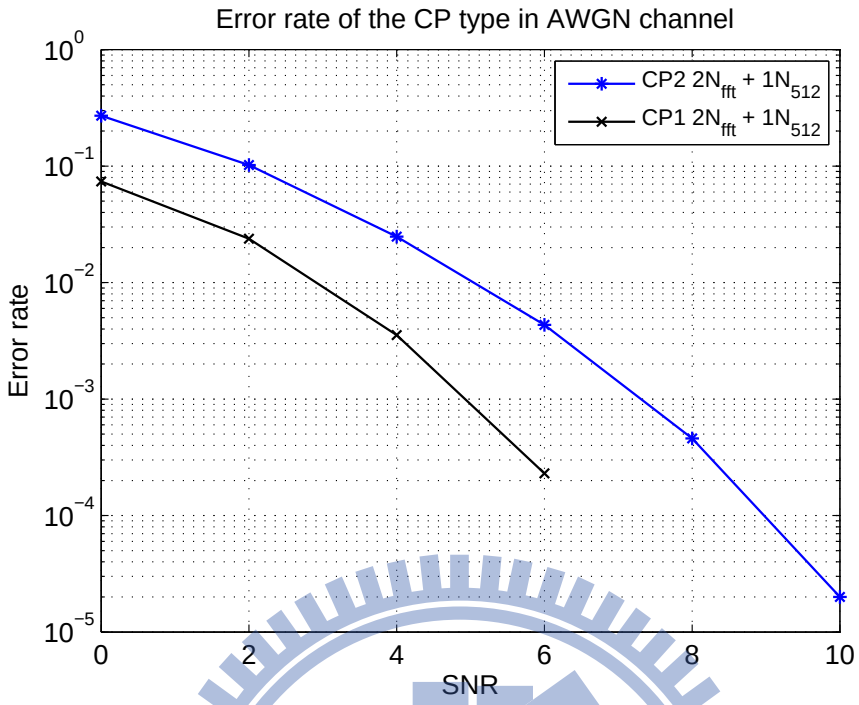

Figure 4.2: Error performance of CP type detection in AWGN channel with window size $2N_{fft} + 1N_{512}$.

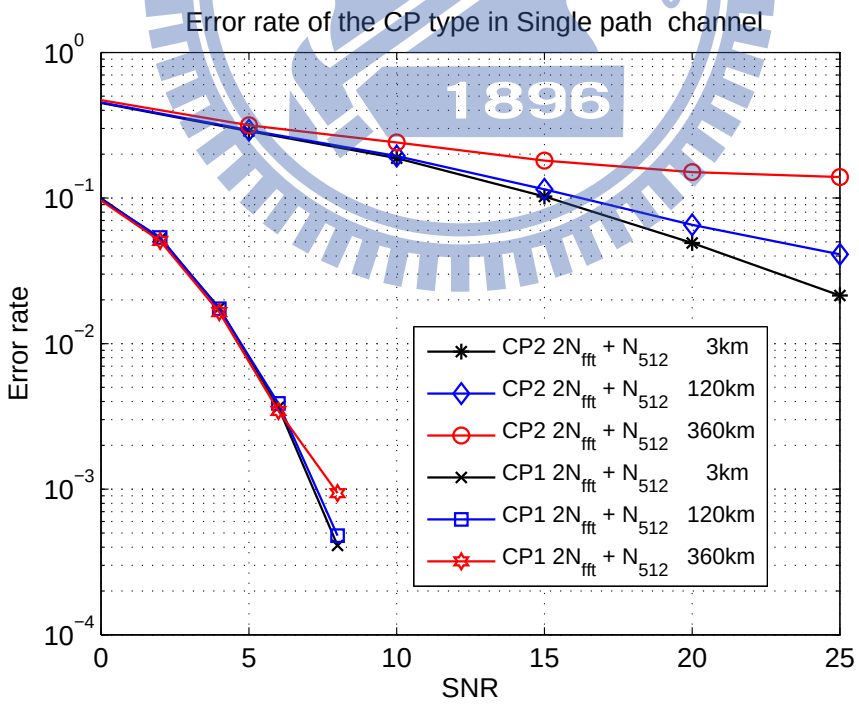

Figure 4.3: Error performance of CP type detection in single-path Rayleigh fading channel at different speeds with window size $2N_{fft} + 1N_{512}$.

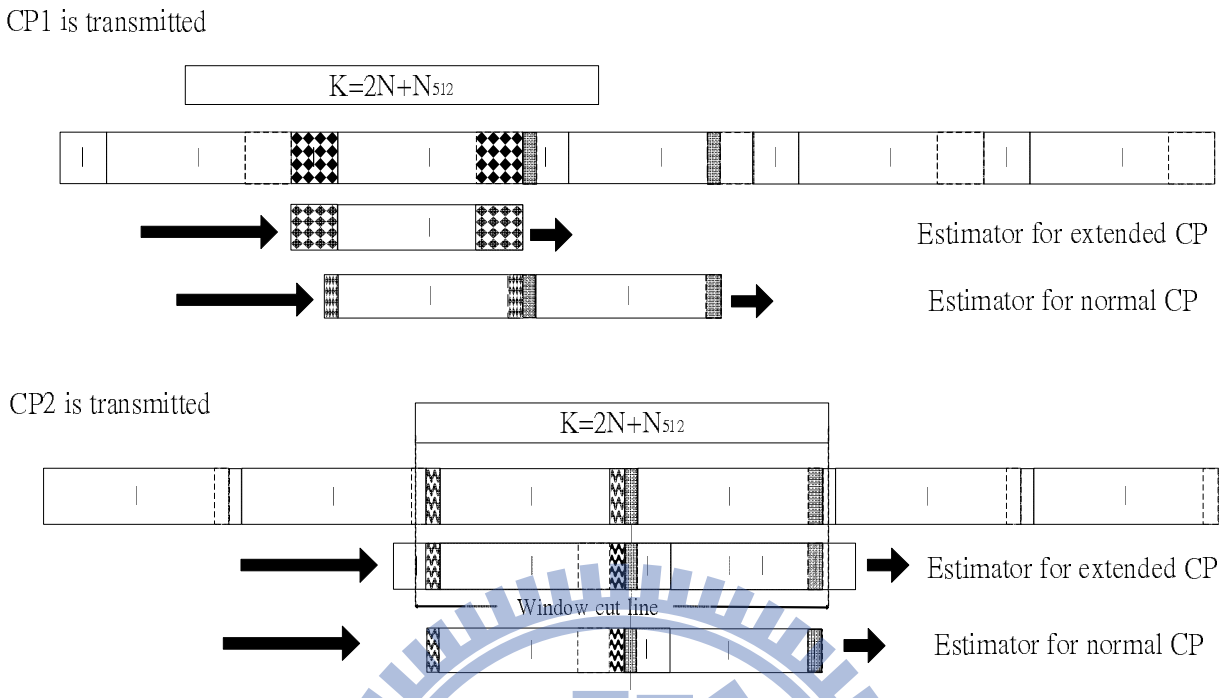

Figure 4.4: Window sliding structure.

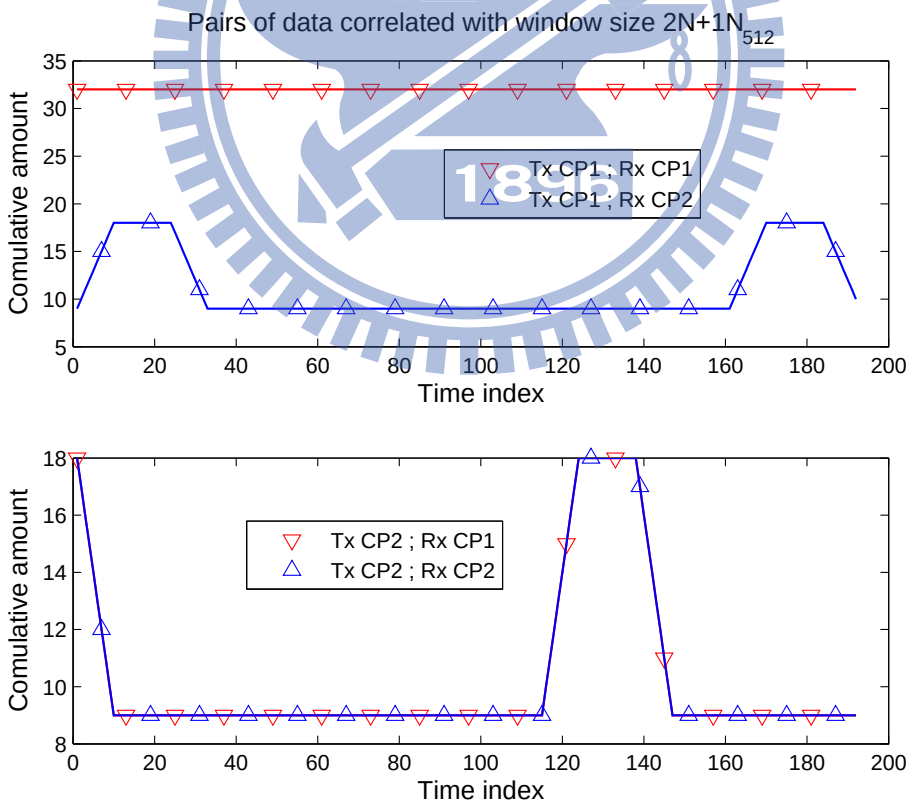

Figure 4.5: Pairs of data correlated with window size $2N_{fft} + 1N_{512}$.

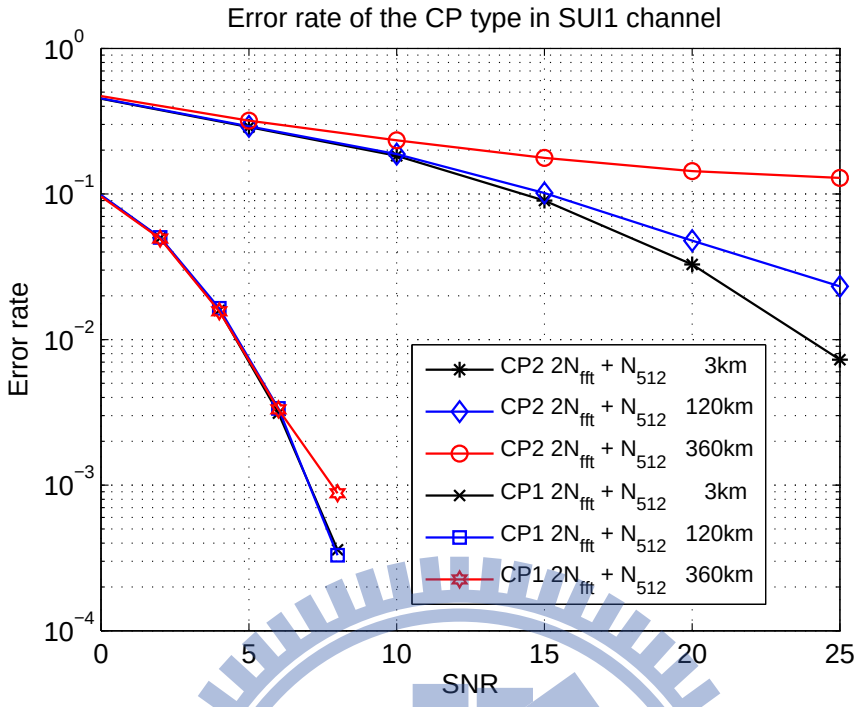

Figure 4.6: Error performance of CP type detection in SUI1 channel at different speeds with window size $2N_{fft} + 1N_{512}$.

pairs of correlated data with different symbol timing index with window size $2N_{fft} + 1N_{512}$. Clearly, the former difference is much larger than the latter. From this point of view, we can see that the most error caused are from transmitting CP2 type.

4.3.2 Multipath Fading Channels

Figures 4.6–4.10 illustrate the simulation results under modified SUI1 to SUI4 and PB channels with different mobility. Still, the error caused by transmitting CP1 type is much less than transmitting CP2 type.

4.4 CP Type Estimation Performance Under Different Observation Window Sizes

In this section, we compare the error rate of CP type under different observation window sizes between $2N_{fft}+1N_{512}$ and $6N_{fft}+5N_{512}$. As the same discussion to the previous case of window size $2N_{fft} + 1N_{512}$. Figure 4.11 shows the numbers of maximum pairs of correlated

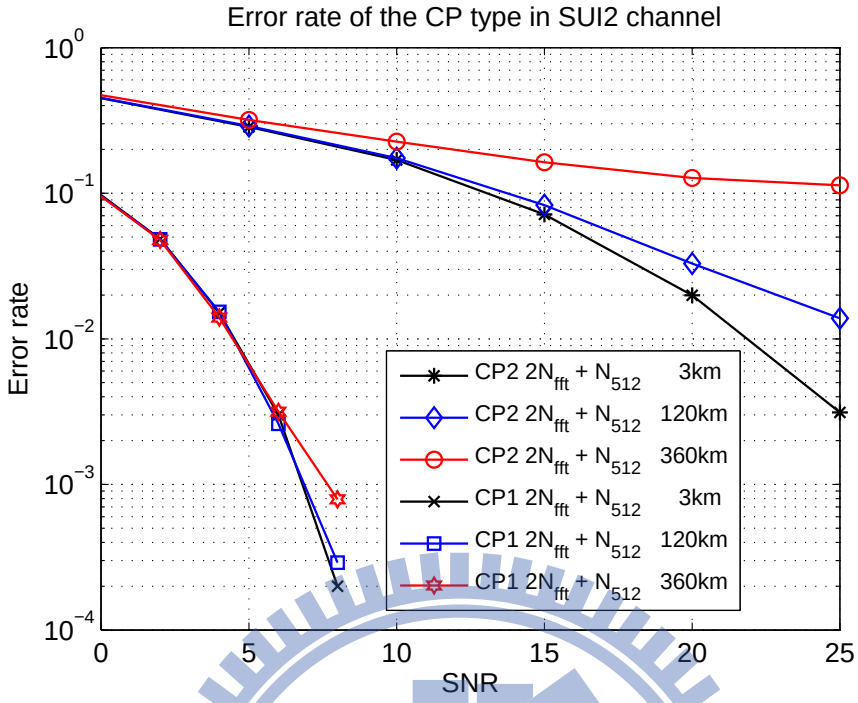

Figure 4.7: Error performance of CP type detection in SUI2 channel at different speeds with window size $2N_{fft} + 1N_{512}$.

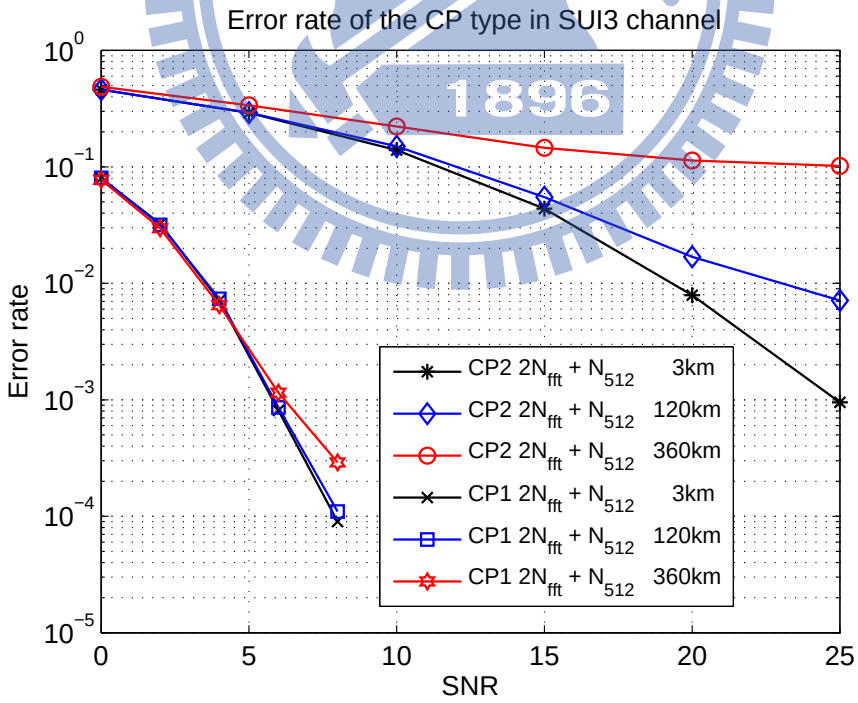

Figure 4.8: Error performance of CP type detection in SUI3 channel at different speeds with window size $2N_{fft} + 1N_{512}$.

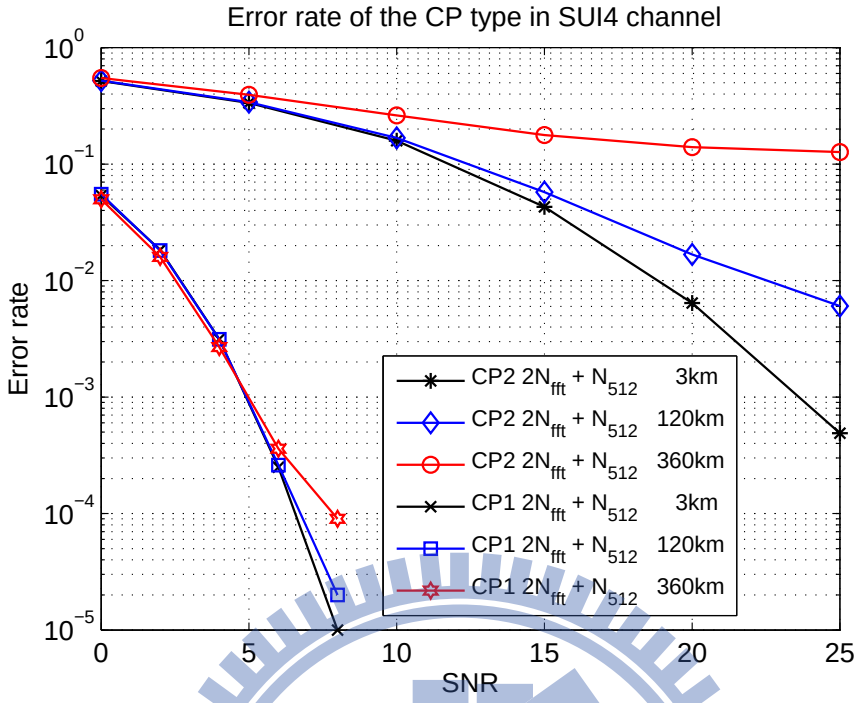

Figure 4.9: Error performance of CP type detection in SUI4 channel at different speeds with window size $2N_{fft} + 1N_{512}$.

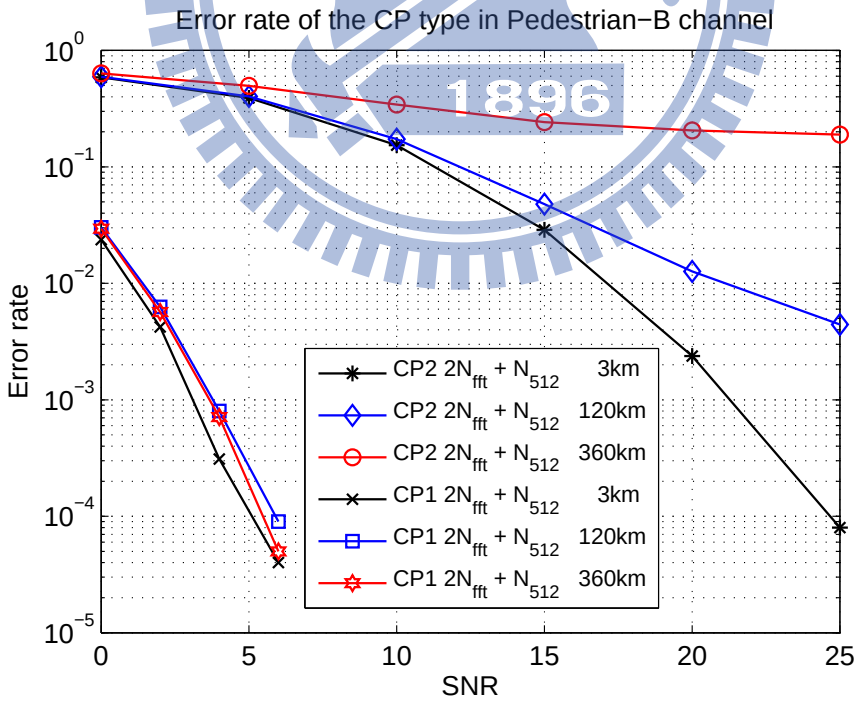

Figure 4.10: Error performance of CP type detection in Pedestrian-B channel at different speeds with window size $2N_{fft} + 1N_{512}$.

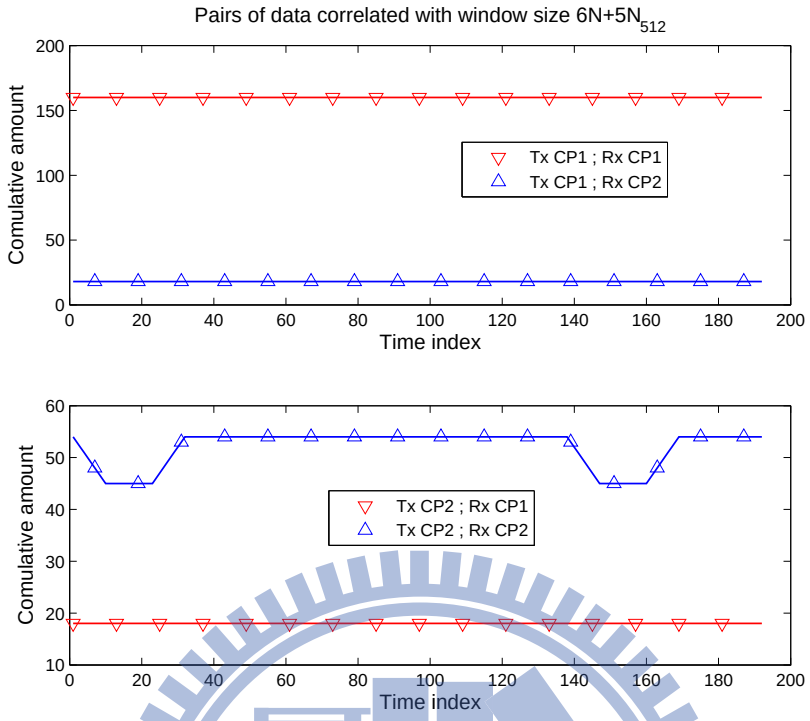

Figure 4.11: Pairs of data correlated with window size $6N_{fft} + 1N_{512}$.

data to different symbol timing index with window size $6N_{fft} + 5N_{512}$. From this figure, we can see that if CP1 type is transmitted, the numbers of maximum pairs of correlated data are always $5N_{512}$ for the CP1 estimator, and they are always $N_{160} + N_{144}$ for the CP2 estimator. The difference is $5N_{512} - (N_{160} + N_{144})$. As CP2 type is transmitted, the numbers of maximum pairs of correlated data are most near $6N_{144}$ for the CP2 estimator, while they are always $N_{160} + N_{144}$ for the CP1 estimator. The difference is $6N_{144} - (N_{160} + N_{144})$. The amount of difference between $6N_{fft} + 5N_{512}$ and $2N_{fft} + 1N_{512}$ in CP1 type is much larger than that in CP2 type, so the performance by using $6N_{fft} + 5N_{512}$ when transmitting in CP1 type improves greater than that in CP2 type. Figures 4.12–4.29 illustrate the simulation results in fading channels under different observation window sizes.

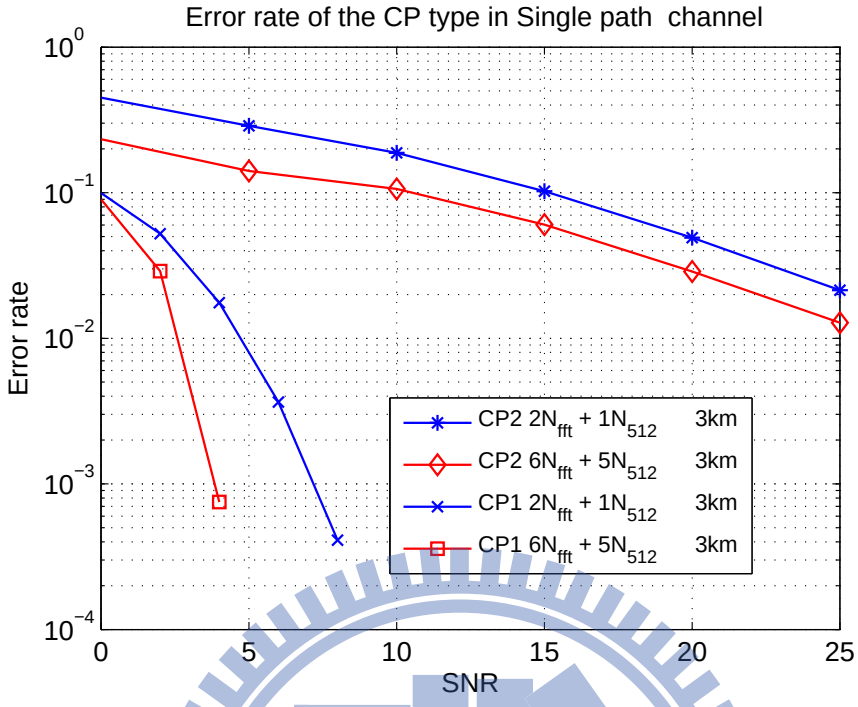

Figure 4.12: Error performance of CP type detection in single-path channel at speed 3 km with several different window size.

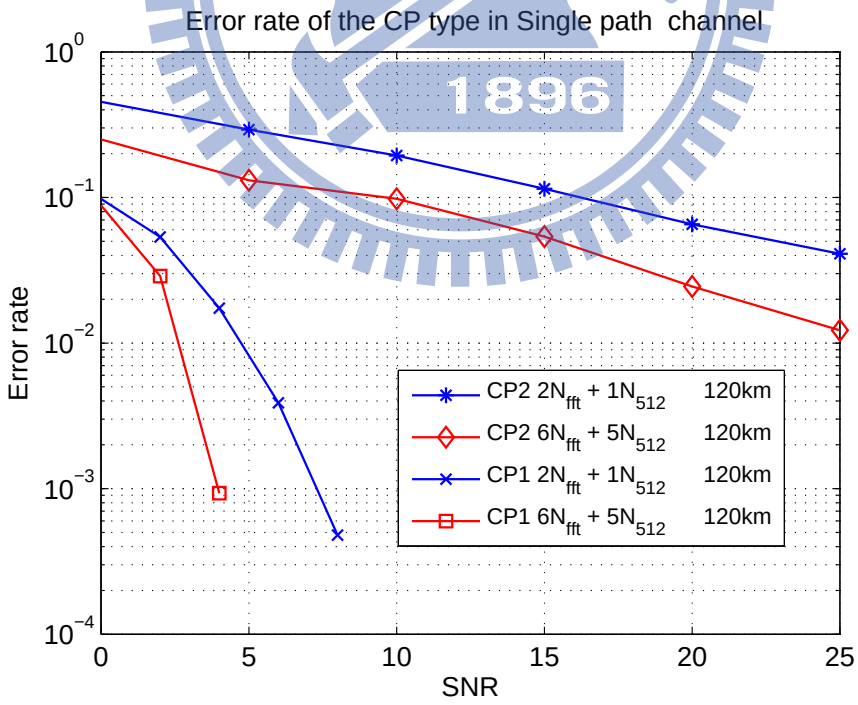

Figure 4.13: Error performance of CP type detection in single-path channel at speed 120 km with several different window size.

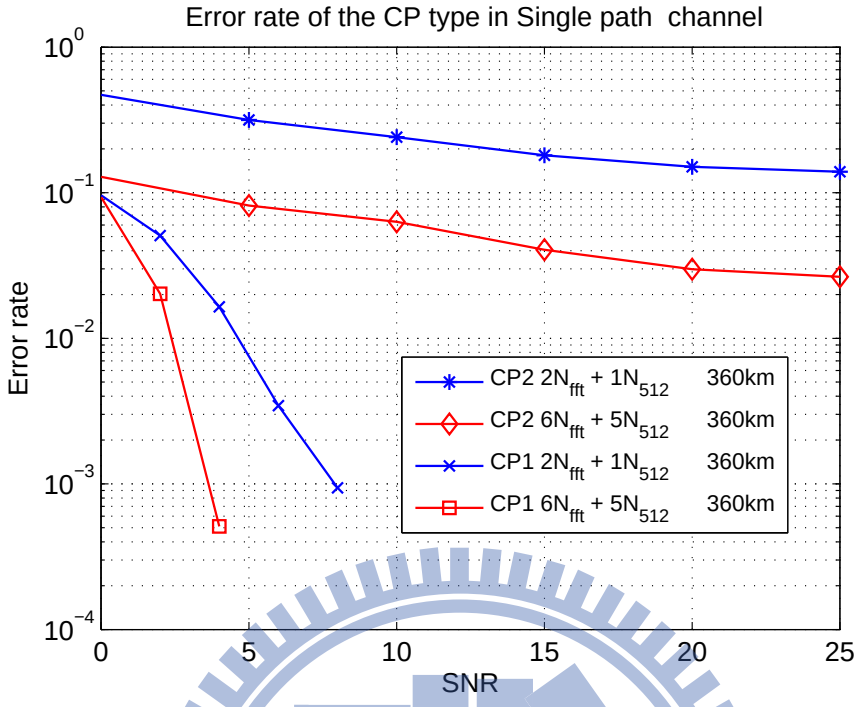

Figure 4.14: Error performance of CP type detection in single-path channel at speed 360 km with several different window size.

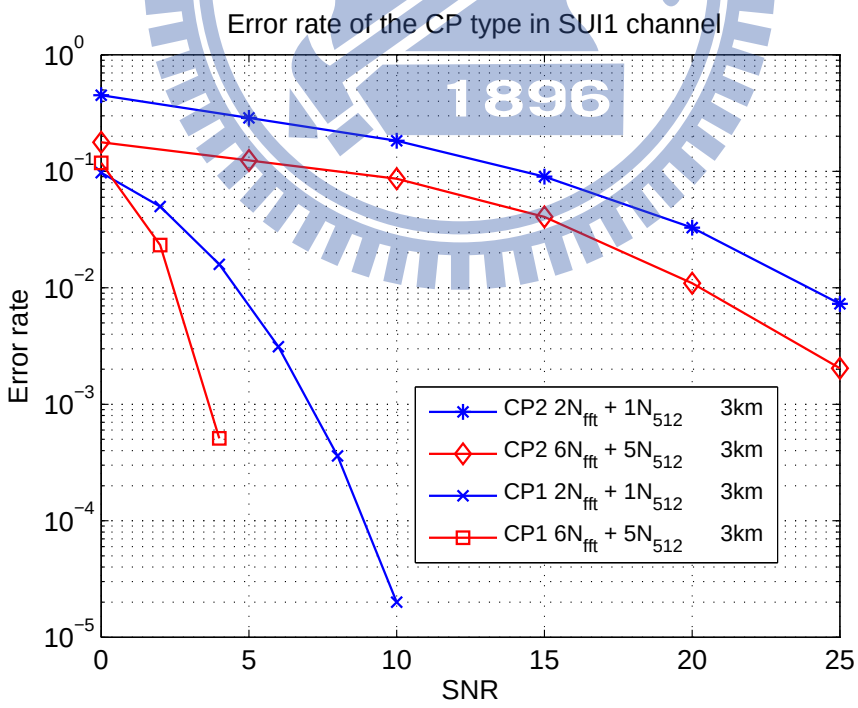

Figure 4.15: Error performance of CP type detection in SUI1 channel at speed 3 km with several different window size.

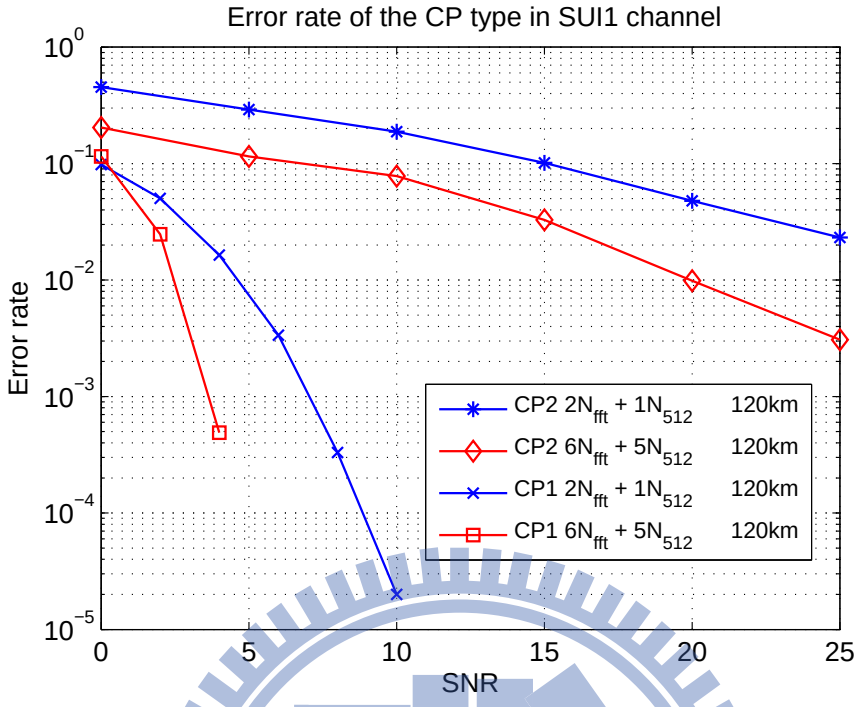

Figure 4.16: Error performance of CP type detection in SUI1 channel at speed 120 km with several different window size.

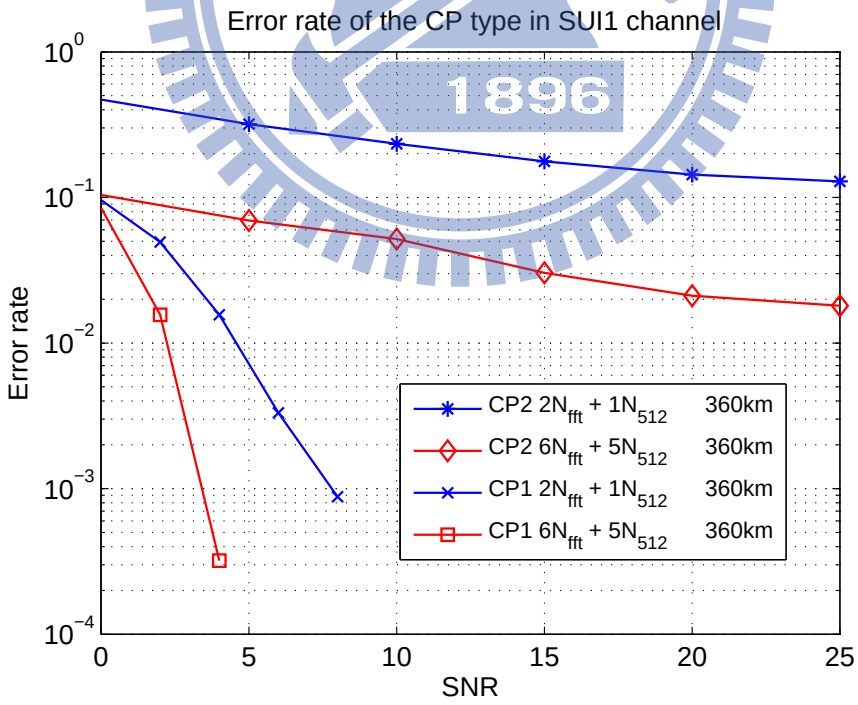

Figure 4.17: Error performance of CP type detection in SUI1 channel at speed 360 km with several different window size.

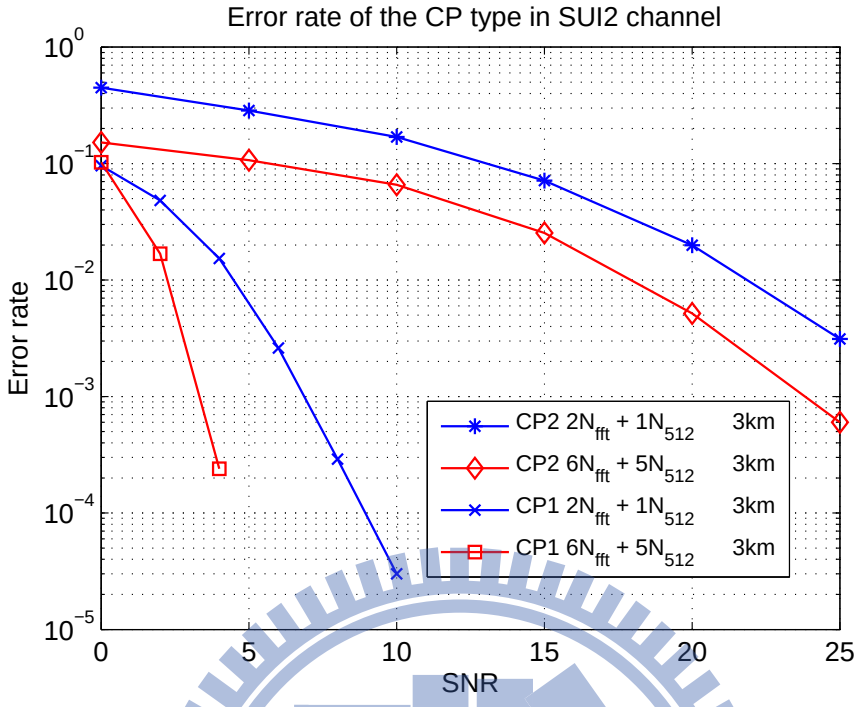

Figure 4.18: Error performance of CP type detection in SUI2 channel at speed 3 km with several different window size.

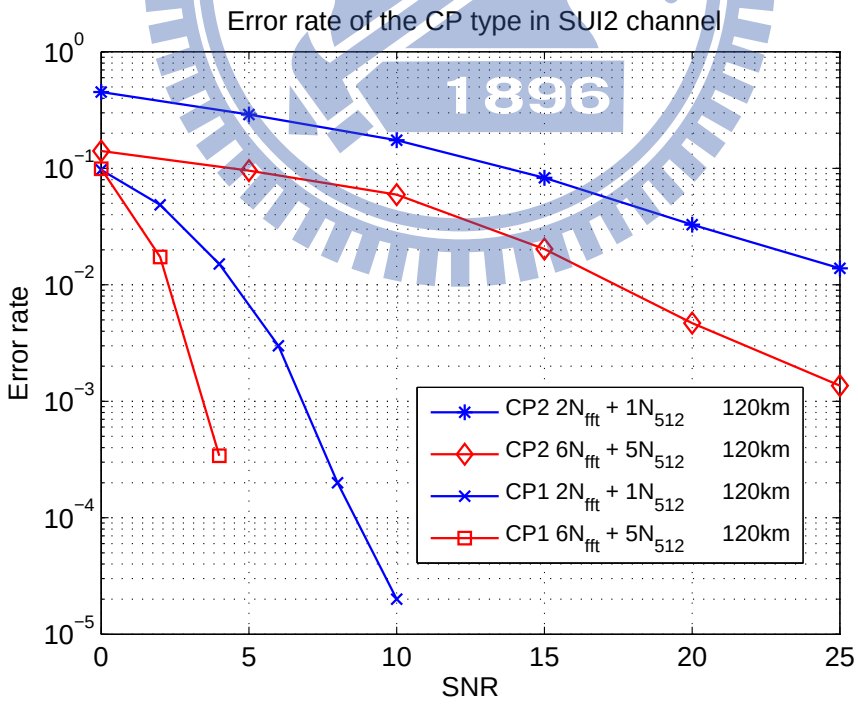

Figure 4.19: Error performance of CP type detection in SUI2 channel at speed 120 km with several different window size.

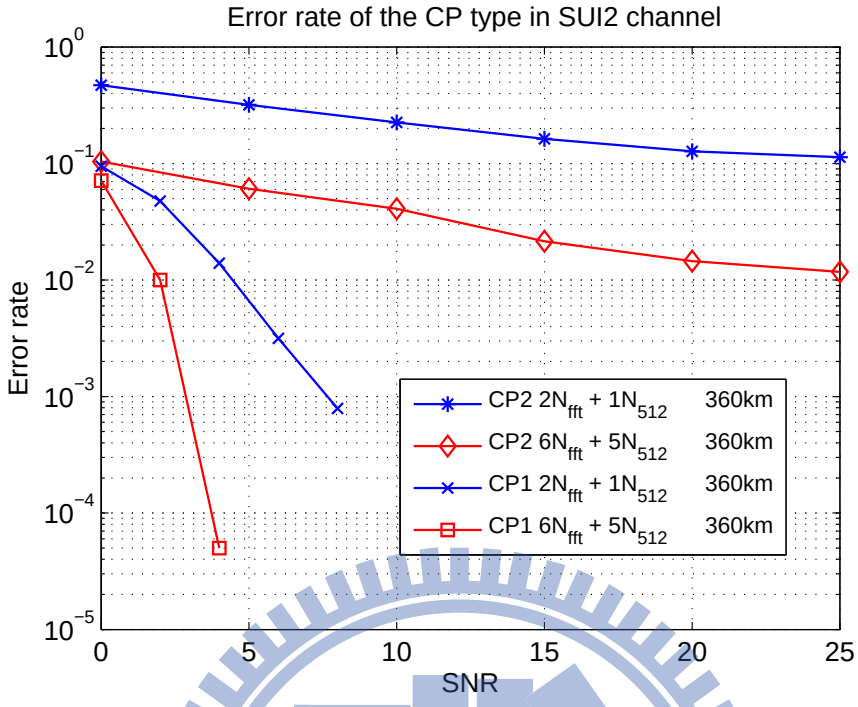

Figure 4.20: Error performance of CP type detection in SUI2 channel at speed 360 km with several different window size.

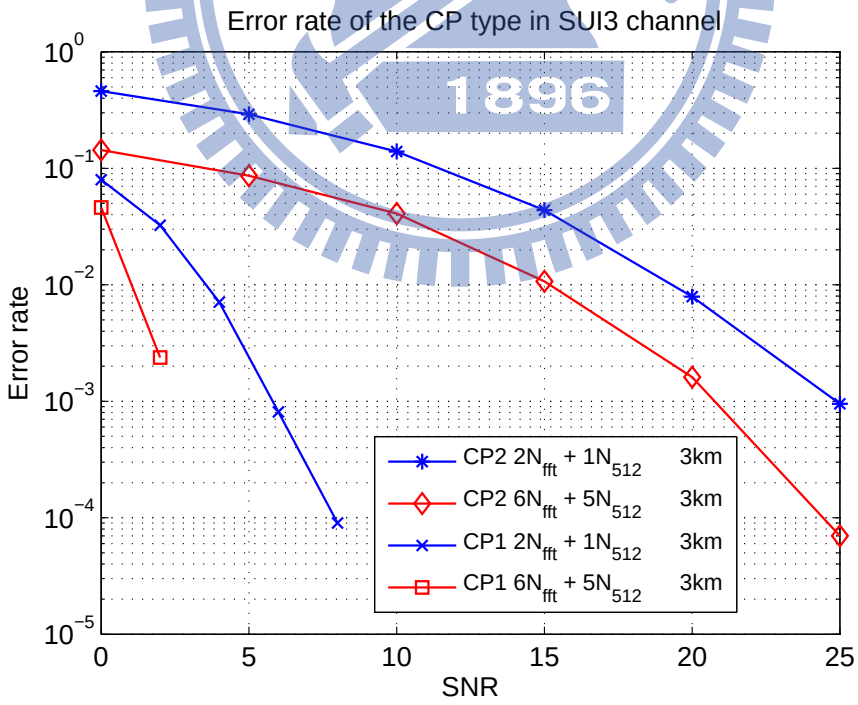

Figure 4.21: Error performance of CP type detection in SUI3 channel at speed 3 km with several different window size.

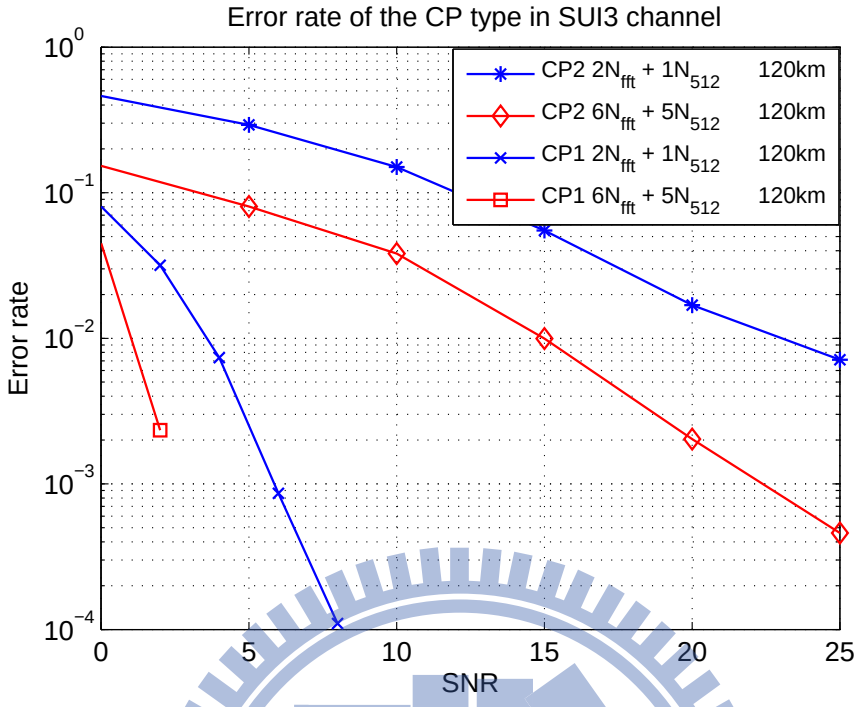

Figure 4.22: Error performance of CP type detection in SUI3 channel at speed 120 km with several different window size.

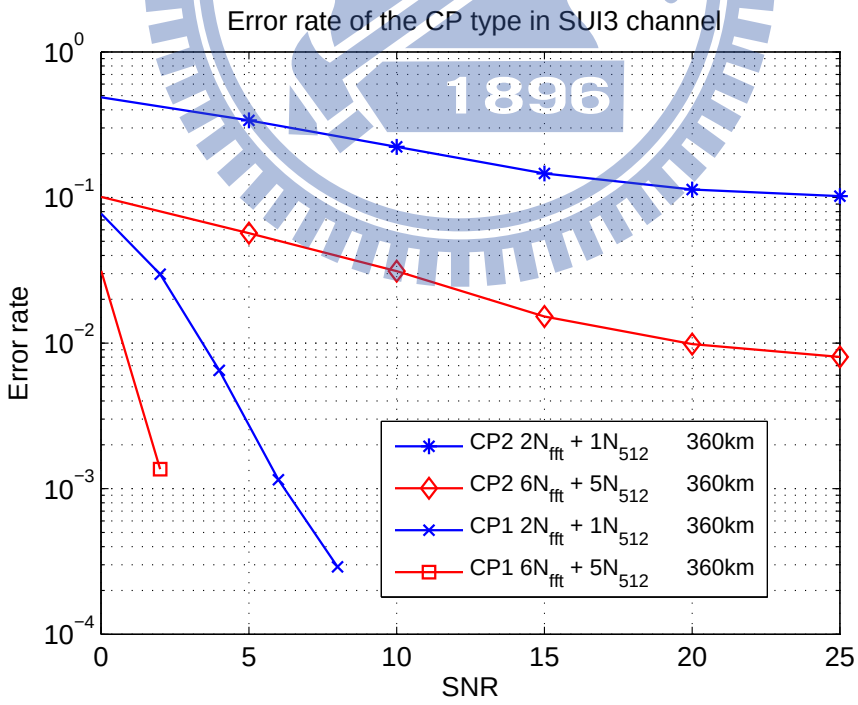

Figure 4.23: Error performance of CP type detection in SUI3 channel at speed 360 km with several different window size.

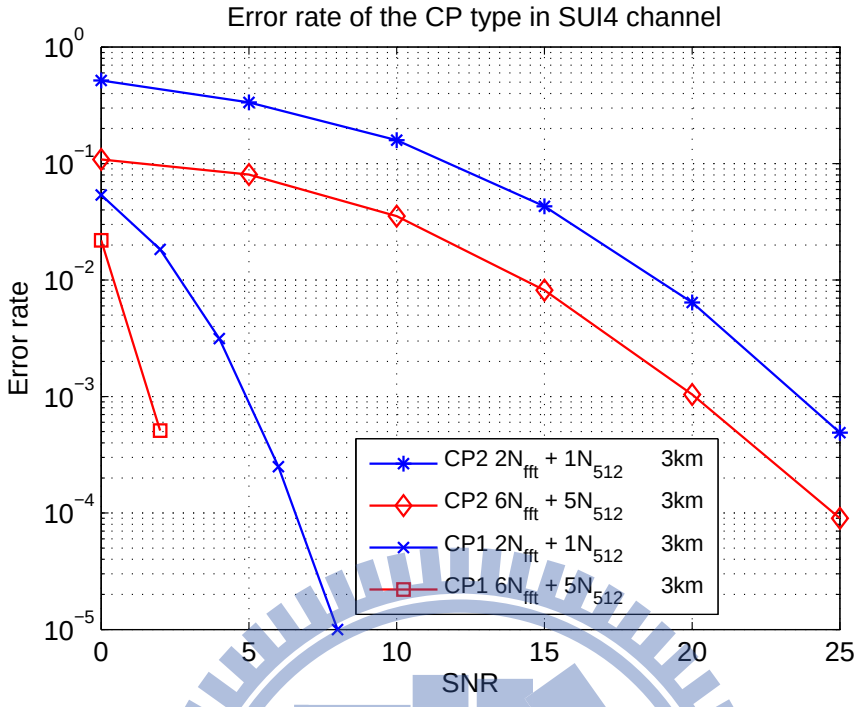

Figure 4.24: Error performance of CP type detection in SUI4 channel at speed 3 km with several different window size.

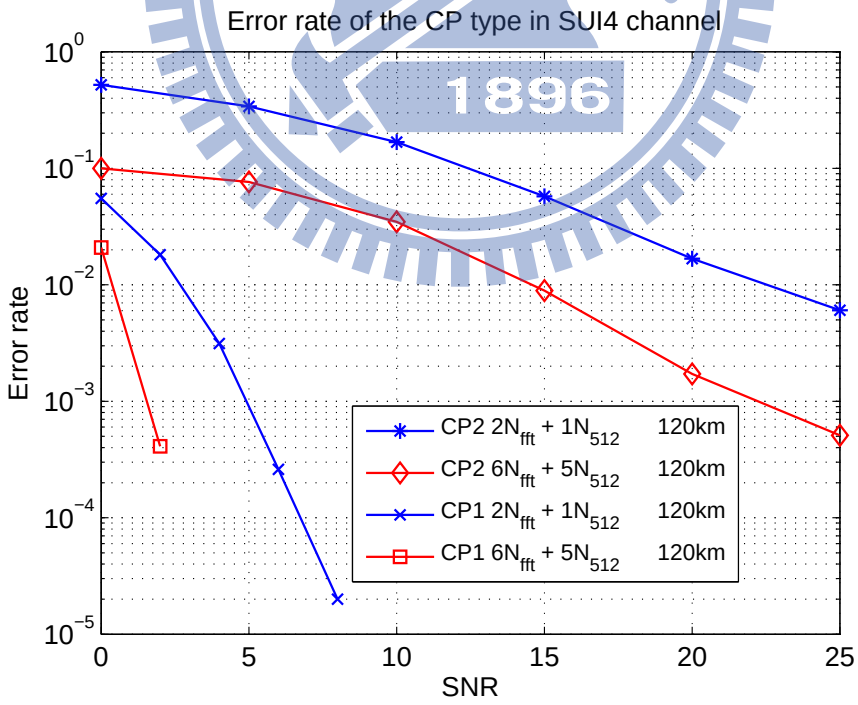

Figure 4.25: Error performance of CP type detection in SUI4 channel at speed 120 km with several different window size.

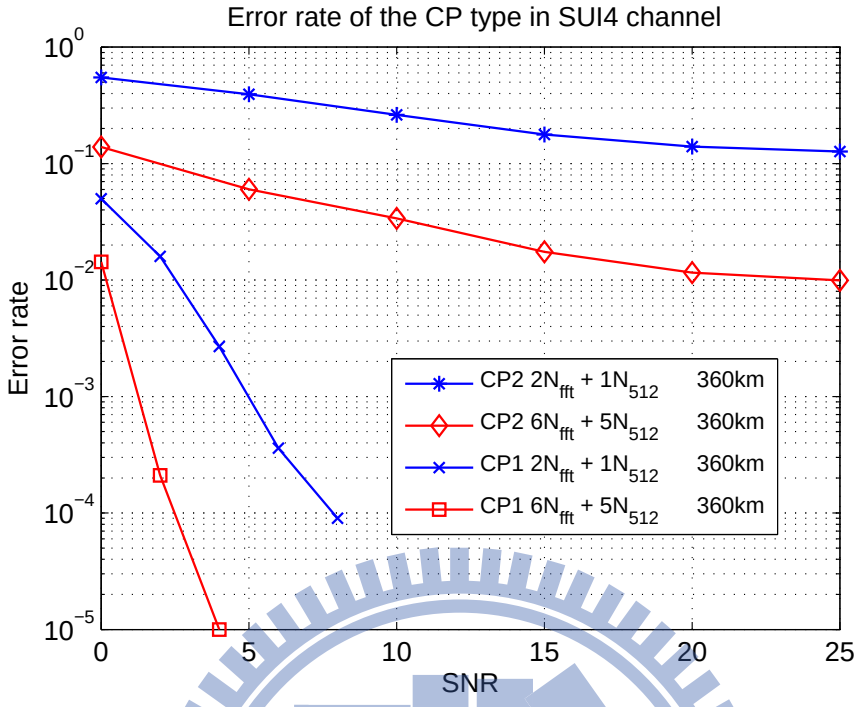

Figure 4.26: Error performance of CP type detection in SUI4 channel at speed 360 km with several different window size.

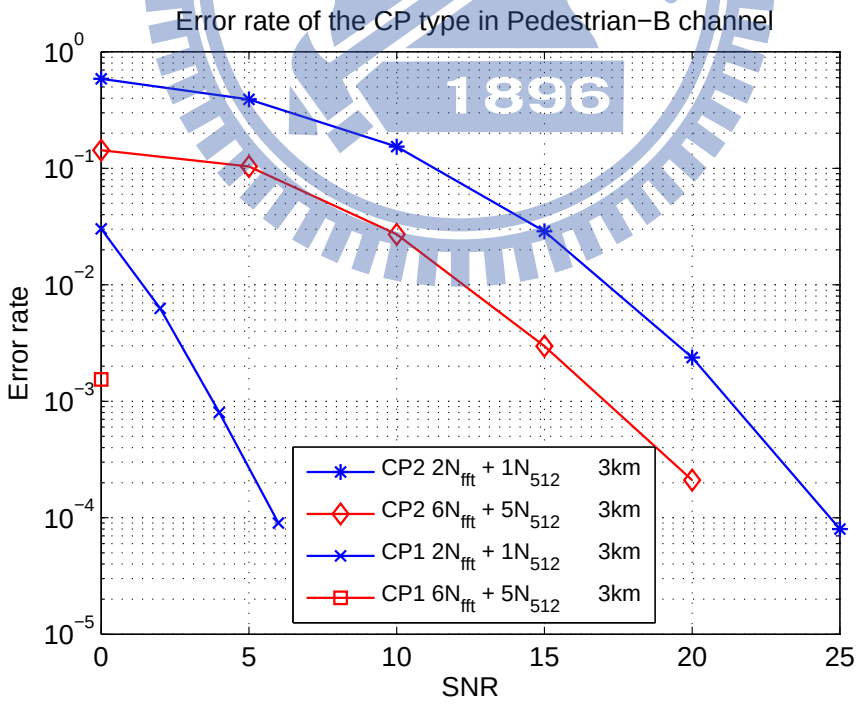

Figure 4.27: Error performance of CP type detection in Pedestrian-B channel at speed 3 km with several different window size.

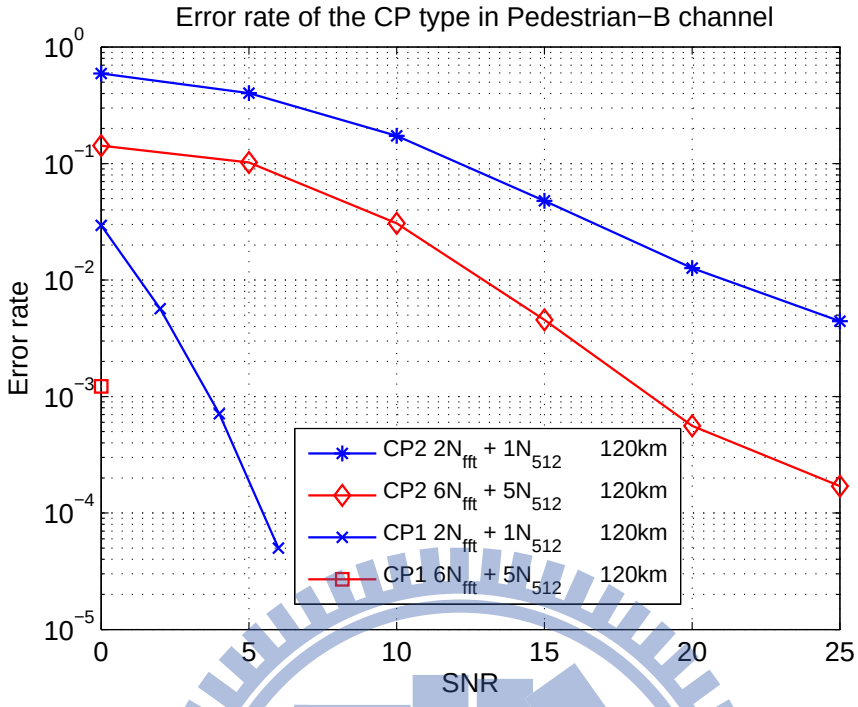

Figure 4.28: Error performance of CP type detection in Pedestrian-B channel at speed 120 km with several different window size.

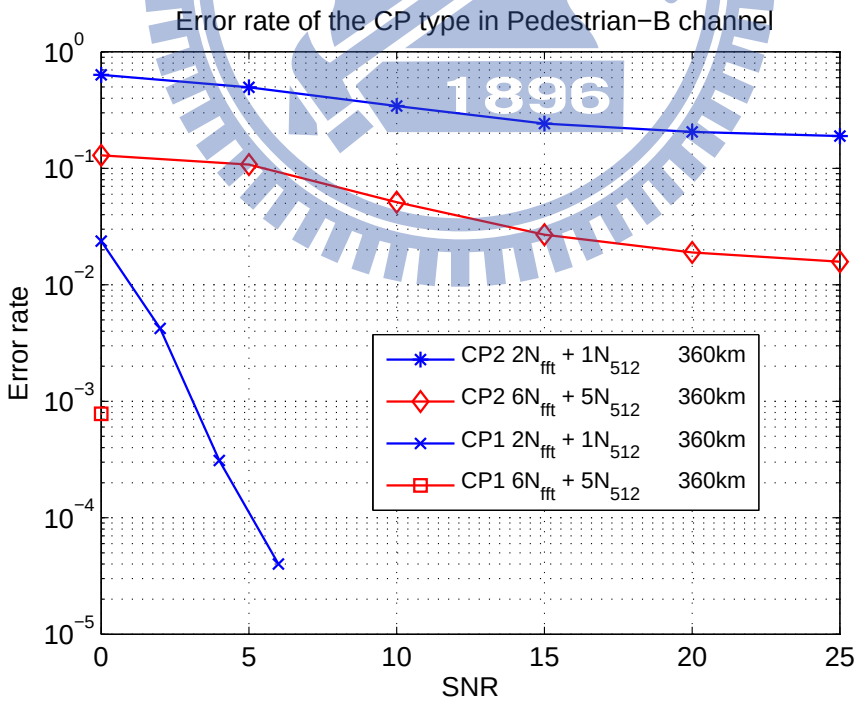

Figure 4.29: Error performance of CP type detection in Pedestrian-B channel at speed 360 km with several different window size.

Chapter 5

Conclusion and Future Work

5.1 Conclusion

The primary contribution in this thesis is to derive the quasi-maximum-likelihood estimator for joint estimation of the CP type, symbol timing offset and carrier frequency offset. It is a generalized solution compared to that proposed in [6], [9] and [10]. The first is only considered in AWGN channel, the second is derived in single-path Rayleigh fading channel, and the last is not an optimal ML estimator due to improper derivation. In estimating carrier frequency offset, we consider an approximation so that it can reduce complexity largely. Though, by doing so, it is the suboptimal solution under multipath fading channels. It is an optimal solution under AWGN and single-path Rayleigh fading channels because the approximate term has no effect on estimation process. There are several advantages in our proposed quasi-ML-estimator.

First, we introduce the parameter K as the observed window size, it allows us to choose the suitable size for estimation compared to that with the fixed window size of 2N+L (CP length) proposed in [6], [9], and [10].

Second, our proposed quasi-ML-estimator is derived ont only based on the AWGN and single-path Rayleigh channel but also the multi-path channel. It will be degenerated to the same result as proposed in [6] and [9] when we consider the AWGN and single-path Rayleigh channel, respectively.

Third, although we use the known PDP of multi-path channel in our simulation, we still reserve it as the parameter in our derivation. If we can deal with the channel estimation at the same time or by doing so with iteration within the several time of symbol timing

duration, we can get the more accurate symbol timing offset and carrier frequency offset, especially.

5.2 Future Work

There are several possible extension for our research:

- Derive the algorithm of the optimal ML estimation with considering the effect of integer CFO by including the primary synchronization sequence (PSS).
- Try to analyze the error rate of CP type in AWGN and single-path Rayleigh channel.
- Take the effect of IQ mismatch and sampling frequency offset into consideration, which is a more practical situation.
- Try to do the channel estimator by using the PSS or pilot to get the better performance.
- In this thesis, we assume the channel length is less than the CP length without considering the influence of inter-symbol interference (ISI). The ISI issue can be involved in the future.
- Try to implement our estimator on DSP.

Bibliography

[1] 3GPP TS 36.211, *"Physical Channels and Modulation,"* V11.3.4, June 2013.

[2] Farooq Khan, *LTE for 4G Mobile Broadband: Air Interface Technologies and Performance.* Cambridge University Press, 2009.

[3] Yong Soo Cho, Jaekwon Kim, Won Young Yang, and Chung G. Kang, *MIMO-OFDM Wireless Communications with MATLAB.* IEEE Press, 2010.

[4] Steven M. Kay, *Fundamentals of Statistical Signal Processing, Volume I: Estimation Theory.* Prentice Hall, 1993.

[5] Steven M. Kay, *Fundamentals of Statistical Signal Processing, Volume II: Detection Theory.* Prentice Hall, 1993.

[6] J.J. van de Beek, "ML estimation of time and frequency offset in OFDM systems," *IEEE Trans. Signal Processing*, vol. 45, no. 7, pp. 1800–1805, July 1997.

[7] Navid Lashkarian and Sayfe Kiaei, "Class of cyclic based estimators for frequency offset estimation of OFDM systems," *IEEE Trans. Commun.*, vol. 48, no. 12, pp. 2139–2149, Dec. 2000.

[8] Yik-Chung Wu and Erchin Serpedin, "Comments on on 'Class of cyclic based estimators for frequency offset estimation of OFDM systems'," *IEEE Trans. Commun.*, vol. 53, no. 3, pp. 413–414, Mar. 2005.

[9] Jia-Chin Lin, "Maximum likelihood frame timing instant and frequency offset estimation for OFDM communication over a fast Rayleigh fading channel," *IEEE Trans. Vehicular Technology*, vol. 52, no. 4, pp.1049–1062, July 2003.

[10] Tiejun Lv, Hua Li, and Jie Chen, "Joint estimation of symbol timing and carrier frequency offset of OFDM signals over fast time-varying multi-path channels," *IEEE Trans. Signal Processing*, vol. 53, no. 12, pp. 4526–4535, Dec. 2005.

[11] Po-Sen Wang, Kai-Wei Lu, David W. Lin, and Pangan Ting, "Quasi-maximum likelihood initial downlink synchronization for IEEE 802.16m," in *IEEE 12th Int. Workshop Signal Process. Advances Wireless Commun.*, June 2011, pp. 521–525.

[12] Young Bum Kim and Kyung Hi Chang, "Complexity optimized CP length pre-decision metric for cell searcher in the downlink of 3GPP LTE system, in *IEEE Int. Symp. Personal Indoor Mobile Radio Commun.*, Sept. 2009, pp. 895–899.

[13] Wen Xu and Konstantinos Manolakis, "Robust synchronization for 3GPP LTE system," in *IEEE Global Telecommunications Conference*, Dec. 2010, pp. 1–5.

[14] Kai-Wei Lu, "Initial downlink synchronization for IEEE 802.16m," M.S. thesis, Industrial Technology R & D Master Program on Communication Engineering, National Chiao Tung University, Hsinchu, Taiwan, R.O.C., Feb. 2010.

[15] http://en.wikipedia.org/wiki/3GPP_Long_Term_Evolution.

作者簡歷

學生謝男鑫，民國七十七年十一月出生於苗栗縣。民國一百年六月畢業於國立交通大學電子工程學系，並於民國一百年九月進入國立交通大學電子研究所，從事 OFDMA 通訊系統方面相關研究。民國一百零二年八月取得碩士學位，碩士論文題目為『以偵測循環字首類型為重點之 LTE 初始下行同步』。